Sustained macrophage reprogramming is required for CD8$^+$ T cell–dependent long-term tumor eradication

Carolina Jardim[1#], Marta Bica[1#], Mariana Reis-Sobreiro[1], Afonso Teixeira da Mota[1], Raquel Lopes[1], Miguel Pinto[1], Neuza Sousa[1], Sofia Mensurado[1], Henning Boekhoff[1], Tommaso Scolaro[1], Maud Reugebrink[1], Natacha Gonçalves-Sousa[1], Hiroshi Kubo[1], Catarina Monteiro Gomes[2,3], Catarina Brito[2,3], Rafael Arguello[4], Elvira P. Leites[1], Vanessa A. Morais[1], Bruno Silva-Santos[1], Nuno L. Barbosa-Morais[1*] and Karine Serre[1,5*]

1 Gulbenkian Instituto para a Medicina Molecular, Faculdade de Medicina, Universidade de Lisboa, Lisbon, Portugal

2 iBET, Instituto de Biologia Experimental e Tecnológica, Oeiras, Portugal

3 Instituto de Tecnologia Química e Biológica António Xavier, Universidade Nova de Lisboa, Oeiras, Portugal

4 Aix Marseille Université, CNRS, INSERM, CIML, Centre d'Immunologie de Marseille-Luminy, Marseille, France

5 GIMM-CARE, Gulbenkian Instituto para a Medicina Molecular, Faculdade de Medicina, Universidade de Lisboa, Lisbon, Portugal

# These authors contributed equally.

* Corresponding authors. Email: Karine Serre karine.serre@gimm.pt; Nuno L. Barbosa-Morais nuno.morais@gimm.pt

Running title: Repeated TAM programming boosts antitumor responses

Authors' disclosures: The authors declare no conflicts of interest.

Funding: This work was sponsored by: LISBOA-01-0145-FEDER-030948, with the project cofunded by Fundo Europeu de Desenvolvimento Regional (FEDER), through POR Lisboa 2020 (Programa Operacional Regional de Lisboa, PORTUGAL 2020) and Fundação para a Ciência e a Tecnologia (FCT); national funds through FCT, under the project UIDP/50005/2020. Personal research contracts to K.S. (CEECIND/00697/2018) and N.L.B.-M. (CEECIND/00436/2018), and PhD fellowships to C.J. (SFRH/BD/144792/2019) and M.B. (2020.05627.BD) were supported by FCT. This study also benefited from Fundo iMM-Laço award grant, and was supported by GIMM-CARE. GIMM-CARE is funded by the European Union's Horizon Europe research and innovation programme under grant agreement No. 101060102. GIMM-CARE is co-funded by the Portuguese Government, the National Foundation for Science and Technology (FCT), the Francisco Manuel dos Santos Society Group (ARICA – Investimentos, Participações e Gestão and Jerónimo Martins), iMM and CAML - Lisbon Academic Medical Centre. This work also benefited from active interactions with the European Cooperation in Science and Technology (COST) Actions BM1404 Mye-EUNITER and CA20117 - *Converting molecular profiles of myeloid cells into biomarkers for inflammation and cancer (Mye-InfoBank)*.

Abstract

Tumor-associated macrophages (TAMs) exhibit a dual role in tumor progression and antitumor immunity. However, understanding the functional states and molecular mechanisms of antitumor TAMs remains a challenge. Herein, we show that intratumoral administration of a combination of agonists against TLR3 and CD40 (hereafter termed myeloid cell treatment, MCT) reprogrammed TAMs *in situ* to adopt a protective antitumor phenotype in an orthotopic mouse breast cancer model, and that this led to tumor regression. Single-cell RNA sequencing of TAMs from different tumor stages and post-MCT revealed a transient antitumor TAM phenotype, present at 12h post-MCT, characterized by markers such as iNOS and CD38, which was replaced by TAMs co-expressing tumor-limiting and promoting features by 72h post-MCT. Maintenance of antitumor TAMs required repeated MCT administration, and this promoted the activation of $CD8^+$ T cells and long-term tumor eradication. Mechanistically, ROS and TNF-α were pivotal in TAM-mediated tumor control. Our findings uncover the vulnerability of transient TAM reprogramming and show that it can be overcome by repeated MCT administrations to sustain efficient antitumor immune responses.

Synopsis

Tumor-associated macrophages (TAMs) typically support tumor growth but can be reprogrammed to an antitumor phenotype. The authors show that repeated administration of TAM-targeting treatments is needed to sustain the reprogrammed antitumoral phenotype, providing translationally relevant insight.

Introduction

Tumor-associated macrophages (TAMs) dominate the immune landscape in solid tumors, and their multifaceted phenotypes influence tumor progression (1). TAMs promote tumor growth, angiogenesis, invasion, metastasis, and immune evasion, complicating therapeutic responses and often leading to poor clinical outcomes (2, 3). Yet, in certain cancers, such as ovarian, $HER2^+$ breast cancer and colorectal cancer, TAMs are associated with improved survival (2, 4, 5).

Historically, macrophages have been segregated into M1 and M2 phenotypes, with M1 macrophages driving antitumor responses and M2 macrophages fostering tumor progression. According to the immune contexture, in various solid cancer types, M1 features are associated with favorable prognosis, while M2 features correlate with poor outcomes (6). However, this simplistic classification fails to capture the full spectrum of macrophage diversity and plasticity in the tumor microenvironment (TME) (7). Single-cell omics assays have uncovered a remarkable heterogeneity among macrophages, unexpectedly revealing the coexistence of M1 and M2 signatures within macrophage clusters (8). This highlights a complexity beyond simple dichotomy underscoring the need to study TAMs longitudinally *in situ* to understand the contextual dynamic diversity of their functional states in the TME.

Most literature focuses on describing TAMs from progressing tumors and emphasizes TAMs that support cancer progression, thus overshadowing that macrophages can also limit tumor growth. Our incomplete understanding of the complex diversity and plasticity of TAMs has hindered the development of monocyte/macrophage-targeting strategies for clinical use. A key challenge is deciphering the molecular mechanisms of antitumor TAM dynamics and phenotypic heterogeneity. A limited number of single-cell RNA sequencing (scRNA-seq) studies have explored antitumor TAMs *in vivo* (9, 10), and efforts are underway to standardize functional annotations (11, 12). Naturally occurring antitumor TAMs are difficult to capture, as they may operate principally in early asymptomatic developing tumors (13, 14). Consequently, the molecular determinants of protective TAM functions, and their dynamics and maintenance mechanisms remain poorly defined.

Here, we demonstrate the potential of combination treatment with TLR3 and CD40 agonists, referred to herein as myeloid cell treatment (MCT), to induce tumor-killing macrophages *in* *vitro* and to promote robust tumor regression *in vivo*, in mice orthotopically transplanted with E0771 breast tumor cells. We found that TAMs controlled tumor growth within the first 3 days post-MCT, and complete and durable tumor eradication required three consecutive MCT injections. To dissect the underlying dynamics and heterogeneity of TAMs, we isolated them from early-stage not-treated tumors (NT), late-stage progressing tumors (PT), and 12h and 72h post-MCT treatment (MCT-12h and MCT-72h, respectively). Using scRNA-seq, we identified an antitumor phenotype in MCT-activated TAMs that was characterized by enhanced expression of inducible nitric oxide (NO) synthase (iNOS) and CD38. These antitumor TAMs were transiently present in the TME and required MCT reinjection for phenotypic and functional maintenance. Furthermore, reactive oxygen species (ROS) and tumor necrosis factor-alpha (TNF-α) acted as potent antitumor effector molecules of MCT-activated TAMs *in vivo*. MCT-induced TAMs promoted tumor immunogenicity and self-antigen presentation through IFN-α/β-dependent mechanisms. Finally, MCT also induced intratumoral accumulation of effector CD8^{+} T cells, which were essential for long-term tumor eradication. Overall, our data support a framework strategy for sustaining antitumor TAMs *in vivo* as to enable durable tumor elimination in cooperation with cytotoxic T lymphocytes.

Materials and Methods

Mice and tumor cell line

C57Bl/6J (B6) wild-type mice, B6.*Rag2*$^{-/-}$$\gamma c^{-/-}$, B6.*Jht*$^{-/-}$, B6.*Il15r*$^{-/-}$, B6.$Tcr\alpha^{-/-}$ and B6.$Tcr\delta^{-/-}$ mice were purchased from Instituto Gulbenkian de Ciencia (Oeiras, Portugal) or Charles River Laboratories International Inc. *Batf3*$^{-/-}$ mice were kindly provided by Dr. Caetano Reis e Sousa (Francis Crick Institute, London, UK) with permission from Dr. Ken Murphy (Washington University School of Medicine, Washington, US). *Nos2*$^{-/-}$ mice were kindly provided by Dr. Margarida Correia Neves (University of Minho, Braga, Portugal). Mice were housed under specific pathogen–free conditions and the genetically modified animals were bred at the Instituto de Medicina Molecular – João Lobo Antunes (iMM-JLA), Lisbon, Portugal, under conventional conditions. Standard food and water were given *ad libitum*. Animals used in experiments were females 5–15 weeks of age, aged-matched within 4 weeks. All experimental procedures followed European Union guidelines, were performed in compliance with the relevant laws and institutional guidelines, and were approved by the institutional animal welfare body – ORBEA-iMM-JLA – and by the Portuguese national authority for animal health – Direcção-Geral de Alimentação e Veterinária (DGAV).

B16F10 (RRID:CVCL_0159, ATCC, 2012), CT26 (RRID:CVCL_7254, ATCC, 2015), E0771 (RRID:CVCL_GR23, Tebu-Bio, 2018) and MC38 (RRID:CVCL_B288, Kerafast, 2017) cell lines were maintained in our laboratory. The LKR cell line was a kind gift from Dr. Zvi Fridlender (The Hebrew University of Jerusalem, obtained in 2018). These cells were not authenticated by our laboratory. All cell lines were grown in Dulbecco's modified Eagles' medium (DMEM) (Gibco; Thermo Fisher Scientific) with 10% (v/v) FCS (Gibco; Thermo Fisher Scientific) and 1% (v/v) penicillin/streptomycin (pen/strep; Sigma/Merck), hereafter referred to as complete DMEM (cDMEM). Stock vials from lower passages were kept at -80 ºC until thaw for each experiment. Tumor cells were tested for mycoplasma contamination regularly (Mycoalert Mycoplasma Detection kit from VWR). After thawing cells were kept at 37°C in a humidified incubator in the presence of 5% CO2 and passaged only once before implantation into mice. For tumor cell injections, E0771 cells at ~70% confluence were detached using TrypLE Express (Gibco; Thermo Fisher Scientific) for 5 min at 37ºC, and cells were resuspended in ice-cold PBS with 50% Matrigel® Growth Factor Reduced (Corning, ref: 356231). For *in vitro* analysis, E0771 tumor cells were prepared as a single-cell suspension for flow cytometry staining, *in vitro* killing assays, *in vitro* MHC-I and self-antigen presentation quantification.

For self-antigen presentation experiments, the E0771 cell line was transduced with a GFP-OVA retroviral vector as previously described (15) or the MSCV-IRES-GFP retroviral vector (RRID:Addgene_20672). For the transduction, $2x10^5$ E0771 cells were plated in a 48-well plate and 8 μg/mL of polybrene (TR-1003-G, Merck Life Science) with 40 μL of retroviral suspension. Plates were centrifuged at 974g for 1h at 31ºC and incubated at 37ºC for more 8h. The E0771-GFP-OVA cell line and the E0771-GFP cell line were then washed with cDMEM and sorted by flow cytometry to guarantee >98% GFP+ cells.

In vivo tumor transplantation and treatments

For the orthotopic breast cancer model, anesthetized mice were injected with $1x10^6$ E0771 cells in a 1:1 mixture of PBS with Matrigel (Corning) subcutaneously (s.c.) in the mammary fat pad of the left flank (16). B16F10 (5 × 104), CT26 (5 × 105), MC38 (1 × 106) or LKR (1 ×

106), were injected s.c. in the flank of mice, in PBS with 50% Matrigel (except B16F10), in a volume of 50 µL. Tumor growth was assessed every 2-3 days using calipers and calculated as (length × width × width)/2. Mice were sacrificed for analysis, by CO_2 narcosis, at different time-points or when tumor size reached a humane endpoint (length of 10mm or ulceration). Mice that did not develop visible tumors were excluded from the study. When tumors reached 50-100mm^3 of volume, mice were treated every 3 days with 50µl of intra-tumoral (i.t.) solution of 50 µg of the TLR3 agonist poly I:C (InvivoGene; tlrl-picw) and 15 µg of an agonistic anti-CD40 (Bio X Cell Cat# BE0016-2, RRID:AB_1107647). Mice were randomized based on their tumor sizes to homogenize the groups.

For *in vivo* monocyte/macrophage depletion, 100 µl of clodronate liposomes (Liposoma B.V.) were injected s.c. and intravenously (i.v.) one day before, one day after and then concurrently with MCT at day 3 (T3) and 6 day 6 (T6). For *in vivo* CD8$^+$ T-cell depletion, 100 µg anti-CD8α (clone YTS169) + 100 µg anti-CD8α (clone YTS156) (kindly provided by Luis Graça (iMM, Portugal)) were injected intraperitoneally (i.p.), and 30µg directly in the tumor (i.t.) one day before the first MCT administration (T0) and then every 5 days. For *in vivo* NK-cell depletion, 200 µg anti-NK1.1 (Bio X Cell Cat# BE0036, RRID:AB_1107737) was injected i.p., and 50µg i.t. one day before the first MCT administration (T0) and then every 5 days. For ROS inhibition, N-acetyl cysteine (NAC; Sigma/Merck) resuspended in PBS (pH = 7) was administrated i.t. at a concentration of 15 mg/kg/mice, one day before MCT and then every other day. For iNOS inhibition, 280µg and 30µg of 1400W (ab120165; Abcam) plus 1mg and 50µg of Aminoguanidine Hydrocloride (AG; ab120123; Abcam) were injected i.p. and i.t., respectively. For TNFα blockade, 250µg and 30µg of anti-mouse TNFα (Bio X Cell Cat# BE0058, RRID:AB_1107764) were injected i.p. and i.t., respectively. iNOS inhibitors and anti-TNFα were administered one day before MCT, concurrently with MCT, one day after MCT, and then only i.t. every other day.

Tumor tissue processing and cell isolation

Tumors resected from mice were cut into small pieces and digested with 1mg/mL collagenase Type I (Worthington), 0.4 mg/mL collagenase Type IV (Worthington) and 10µg/mL DNase I (Sigma-Aldrich) for 30 min at 37°C, in Eppendorf tubes. Cell suspensions were then filtered through a 100µm nylon cell strainer (Corning). Red blood cells were lysed using RBC Lysis

Buffer (Biolegend) for 10 min at RT in the dark. Cells were centrifuged and resuspended in completeRPMI (cRPMI) (RPMI + Sodium Pyruvate (100x) + Non Essential Acids Amines (100x) + Hepes (100x) + pen/strep (100x) + βMercaptoethanol (1000x) + FCS 10% all from Gibco; Thermo Fisher Scientific) and immediately processed for the specific readout.

Generation of bone marrow–derived macrophages (BMDMs)

BMDMs were derived from haematopoietic progenitors flushed from two femurs with 10ml syringe and 0,5mm needles filled with RPMI 1640 supplemented with 10% (v/v) FCS, 0,2% (v/v) pen/strep and 50 ng/ml macrophage-colony stimulating factor (M-CSF, Peprotech) (BM-medium hereafter). BM cell suspension was filtered through a 100 μm nylon cell strainer (Falcon/Corning) and $4x10^6$ BM cells were seeded in petri dishes (1.6502055, PS estéril, 90mm, Normax) with BM-medium for 6 days, at 37ºC with 5% CO_2. On day 6 BMDM were mechanically detached from the petri dishes using a cell scraper (P21040, ABDOS LifeScience), and $2x10^6$ cells were distributed per well in a 6-well plate. On day 7, BMDMs were polarized for 6 or 24h, at 37ºC with 5% CO_2, with the following conditions: M0 – unstimulated; M1 – lipopolysaccharide (LPS, 50ng/ml, (InvivoGene) + IFNγ (50ng/ml, PeproTech); M2a – IL-4 (50ng/ml, PeproTech) + IL-13 (50ng/ml, PeproTech); and MCT – Poly I:C (10μg/ml, InvivoGene; tlrl-picw) + agonistic anti-CD40 (5μg/ml, InVivoMab, FGK4.5; Bio X Cell Cat# BE0016-2, RRID:AB_1107647). Supernatants of these BMDM were collected and stored at $-20C^0$ until further use. For analysis, BMDMs were mechanically detached from the 6-well plates, washed with PBS and $1x10^5$ macrophages were distributed per well in a 96-well V-bottom plate. Cell viability and phenotype were assessed by flow cytometry.

Flow cytometry and cell sorting

Prior to staining, cells were incubated with mouse FcγIII/II receptors (CD16/CD32) blocking antibody (clone 93; eBioscience) at 1:200 in cRPMI for 10 min. Cell viability was assessed by Zombie Aqua™ Fixable Viability Kit at 1:400 (Biolegend, 423101), or 7-AAD (Biolegend) at 1:1000 for 20 min at 4 °C. Reduced glutathione (GSH) intracellular level was assessed using ThiolTracker violet (Invitrogen;T10095). For surface staining, cells were incubated in the dark for 30 min at RT with the following fluorophore-conjugated antibodies: anti-Ly6C (HK1.4; Thermo Fisher Scientific Cat# 53-5932-82, RRID:AB_2574427; 1:400), anti-F4/80 (BM8;

Thermo Fisher Scientific Cat# 25-4801-82, RRID:AB_469653; 1:200), anti-CD3ε (17A2; Thermo Fisher Scientific Cat# 47-0032-82, RRID:AB_1272181; 1:200), anti-CD3ε (145-2C11; BioLegend Cat# 100327, RRID:AB_893320; 1:100), anti-CD4 (RM4-5; BioLegend Cat# 100547, RRID:AB_11125962; 1:200), anti-CD8a (53-6.7; Thermo Fisher Scientific Cat# 67-0081-82, RRID:AB_2662351; 1:300), anti-CD45 (30-F11; BioLegend Cat# 103146, RRID:AB_2564003; 1:500), anti-CD11b (M1/70; BioLegend Cat# 101222, RRID:AB_493705; 1:400), anti-NK1.1 (PK136; BioLegend Cat# 108723, RRID:AB_830870; 1:200), anti-CD19 (6D5; BioLegend Cat# 115530, RRID:AB_830707;1:200), anti-CD38 (T10; BioLegend Cat# 102719, RRID:AB_10613289; 1:100), anti-Ly6G (1A8; BioLegend Cat# 127639, RRID:AB_2565880; 1:200), anti-CD11c (N418; BioLegend Cat# 117349, RRID:AB_2563905; 1:200), anti-I-A/I-E (MS/114.15.2; BioLegend Cat# 107645, RRID:AB_2565977; 1:2000), anti-PDL1 (10F.9G2; BioLegend Cat# 124319, RRID:AB_2563619; 1:200), and anti-PDL2 (TY25; BioLegend Cat# 107210, RRID:AB_2566345; 1:500).

For intracellular staining, cell suspensions were re-stimulated in the presence of 50ng/ml LPS (InvivoGene; tlrl-pb5lps) and 50ng/ml mouse recombinant IFN-γ (Peprotech) for myeloid cell analysis or with 200ng/ml phorbol 12-myristate 13-acetate (PMA; Sigma/Merck) and 1μg/mL ionomycin (Sigma/Merck) for lymphoid cell analysis. This re-stimulation was for 3-4 hours at 37°C, 5% CO_2 in the presence of 5 μg/ml brefeldin-A (Sigma/Merck) and 2 μM monensin (eBioscience/Thermo Fisher Scientific). Note that, for iNOS detection, similar results were obtained by intracellular staining with or without myeloid re-stimulation. Following re-stimulation, Fc receptor blockade, cell surface staining, and cell viability analysis were performed as described in the prior paragraph. Then, cells were fixed for 1h with fixation/permeabilization buffer from Foxp3/transcription factor staining Buffer (eBioscience™) at 4ºC, followed by intracellular staining in permeabilization buffer (eBioscience™) for 45 min at RT or overnight at 4ºC, with the following fluorophore conjugated antibodies anti-IFN-γ (XMG1.2; Thermo Fisher Scientific Cat# 25-7311-82, RRID:AB_469680; 1:100), anti-TNF-α (MP6-XT22; Thermo Fisher Scientific Cat# 48-7321-82, RRID:AB_1548825; 1:100), and anti-NOS2 (CXNFT; Thermo Fisher Scientific Cat# 12-5920-82, RRID:AB_2572642; 1:100). Finally, cells were washed twice with permeabilization buffer (eBioscience™), filtered with 70μm nylon strainers and immediately analyzed.

For Annexin V staining, cells were washed with PBS and resuspended in annexin V binding buffer and APC Annexin V Apoptosis Detection kit (Biolegend) following the manufacturer's instructions.

Cells analyzed by flow cytometry were acquired on LSR-Fortessa (BD Bioscience) using BD FACSDiva Software (BD Bioscience Versions from 8.0.3 up to 9.4), sorted on a FACS Aria III or FACS Aria Fusion (BD Biosciences) and data were analyzed using FlowJo software V10.9 (BD Biosciences).

scRNA-seq data generation and analysis

Single cell library preparation

Live $CD45^{+}CD19^{-}CD3^{-}NK1.1^{-}$ cells were sorted by flow cytometry from not-treated and MCT-treated tumor-bearing animals. Cells were isolated in 4 independent experiments. Each group (NT, MCT-72h, PT) included a minimum of three samples from distinct biological replicates, except for MCT-12h, which had two biological replicates. To integrate the four groups and mitigate potential batch effects, we included an NT sample in each FACS-sorting session. For each condition, isolated tumor-infiltrating immune cells were derived from two to four independent animals. Cell concentration and viability of each sample were determined using 0.4% trypan blue (Gibco™: 15250061). Cells were washed and resuspended in 1x PBS (calcium and magnesium free) containing 0.04% BSA, to a final concentration of 1,000 cells/µl. In brief, 8,000 to 10,000 cells per condition were loaded onto a 10X Genomics Chromium platform for Gel Bead-in-Emulsion (GEM), complementary DNA (cDNA) generation was performed, and sequencing libraries created with cell- and transcript-specific barcodes, using the Chromium Next GEM Single Cell 3' Kit v3.1 (10× Genomics: PN-1000130), Chromium Next GEM Chip G Single Cell Kit (10× Genomics: PN-1000127) and the Dual Index Kit TT Set A (10× Genomics: PN-1000215), following the supplier's protocol. Libraries were sequenced using the Illumina NovaSeq6000 PE150 targeting 50,000 reads per cell, using services at Novogene (Cambridge, UK).

Data processing

Feature-barcode matrices were generated by aligning reads to the mouse genome (GENCODE vM23/Ensembl 98) using CellRanger software. Specifically, CellRanger v3.1.0 was used for samples S1 through S9, and CellRanger v7.0.1 was used for samples MCT1, MCT3, and NT1. A total of 48,934 cells were imported into R (version 4.1.2), merged, and processed collectively. Quality filtering was performed by retaining only cells that met the following criteria: a minimum library size of 3,162 unique molecular identifiers (UMIs), a minimum of 3,000 expressed genes, and mitochondrial gene content below 25%. We identified and removed doublets using the scDblFinder package (version 1.8.0, https://bioconductor.org/packages/release/bioc/html/scDblFinder.html). The final dataset, encompassing the entire tumor-infiltrating immune cell populations, was 40,446 cells. We employed the scran package (version 1.22.1, https://bioconductor.org/packages/release/bioc/html/scran.html) to normalize library size biases resulting from variations in sequencing depth per cell. We utilized the limma package (version 3.50.3, https://bioconductor.org/packages/release/bioc/html/limma.html) for batch effect correction. Specifically, we employed the removeBatchEffect function to mitigate unwanted batch effects associated with the technical variable "dataset".

Dimensionality reduction and clustering analysis

We performed the following analysis using the Seurat package (version 4.1.1, https://satijalab.org/seurat/) unless mentioned otherwise. We selected the top 4,000 highly variable genes (HVGs) using the FindVariableFeatures function with the selection method set to "vst". We performed principal component analysis (PCA) using the selected highly variable genes (HVGs). We then utilized the top 25 principal components (PCs) to construct t-SNE and UMAP plots. We conducted the clustering analysis using shared nearest neighbor (SNN) modularity optimization based on the top 25 PCs. To identify biologically meaningful clusters, we employed a range of resolutions from 0.1 to 2, with a step size of 0.1. We utilized the clustree package (version 0.5.0, https://cran.r-project.org/web/packages/clustree/index.html) to generate clustering trees illustrating the relationship between clusters across different resolutions. This facilitated the identification of clearly distinct clusters and those that were unstable. Final cluster assessment was conducted by examining the expression of specific markers in each cluster.

Macrophage subset analysis

In the analysis of the full dataset, we identified two major clusters of macrophages by inspecting the differentially expressed genes against the remaining cells. These clusters exhibited upregulation of canonical markers associated with monocytes/macrophages. This group comprised 23,453 cells. Subsequently, we repeated the upstream analysis pipeline for this subset with the following modifications: we selected the top 3,000 HVGs, and we corrected the batch effect associated with the technical variable "sorting".

Differential expression analysis

We conducted differential gene expression analysis on the normalized dataset using the FindAllMarkers/FindMarkers function from the Seurat package. Specifically, we employed the MAST differential expression test for differential gene expression of the clusters (cluster-based analysis) on each subset.

Gene Set Enrichment Analysis

We used the fgsea package (version 1.20.0, https://github.com/ctlab/fgsea) for pathway enrichment analyses. Each analysis involved the following steps: i) we conducted the MAST test for differential gene expression implemented in the Seurat package; ii) to minimize exclusions from the analysis, we set the threshold for log2-fold change (logfc.threshold) to 0; iii) genes were ranked based on their log2-fold change values; iv) we provided this ranked gene list alongside the hallmark pathways from the Mouse MSigDB Collections (https://www.gsea-msigdb.org/gsea/msigdb/mouse/collections.jsp) as inputs to the fgsea function to compute the normalized enrichment score (NES) for each hallmark pathway. Briefly, we ranked the genes based on their absolute log2-fold change values. This approach ensured the inclusion of all genes involved in the pathway, regardless of whether they were up- or down-regulated in the group of interest. After performing gene set enrichment analysis (17), we identified the leading edge genes, i.e., the genes that contributed to the normalized enrichment score for each hallmark pathway of interest.

Tumor killing assay

To evaluate the direct killing properties of BMDM, E0771 tumor cells were stained with CellTrace™ CFSE Cell Proliferation Kit (Life Technologies) 1uM for 15 min at RT, and washed twice with PBS. BMDM of each phenotype (M0, M1, M2, and MCT) were seeded with CFSE E0771 tumor cells at an effector-to-target ratio of 5:1 (BMDM:E0771) in a 96-well flat bottom plate at 37ºC, 5% CO_2 for 48h. Cells were stained with annexin V, 7-AAD, and fluorescent anti-CD11b as described in the Flow cytometry section.

To evaluate the indirect killing properties of BMDM, 100µl of each BMDM supernatant (M0, M1, M2 and MCT) was added to E0771 tumor cells previously seeded at $1x10^4$ cells in cDMEM in 96-well flat bottom plates for 2/3h to allow adherence. After 72h incubation, the medium was removed and replaced with 80µl of CellTiter-Blue® Cell Viability Assay (ref: G8080; Promega) diluted 1:20 in cDMEM and cells were incubated for 1h. Cell viability was read using Microplate Reader Tecan Infinite M200, with the following parameters: 10s orbital shaking, 590nm excitation and 560nm emission of fluorescence.

In another type of experiment, $5x10^4$ E0771 cells were seeded in cDMEM in a 24-well plate overnight, then the medium was replaced with BMDM supernatants (M0, M1, M2, and MCT). After 48h cells were stained with annexin V and 7-AAD as described in the Flow cytometry section.

Tumor immunogenicity Assay

Ten thousand GFP-pMIG or GFP-OVA-vector E0771 cells were incubated in 96-well flat bottom plates in the presence of 100µl of BMDM supernatant (M0, M1, M2 and MCT) with or without 5 µg/ml of anti-TNFα (XT3.11; InVIvoMab), 5 µg/ml of anti-IFNγ (XMG1.2) or 5 µg/mL of anti-IFNα/βR (MAR1-5A3; Selleckchem) for 24h. Then, cells were detached and surface staining with fluorophore conjugated anti-H-2Kb (AF6-88.5; 1:100) or anti-SIINFEKL H-2Kb (25-D1.16;1:100), both from Biolegend, was performed as described in the flow cytometry section.

SCENITH™

One hundred thousand polarized BMDMs were seeded in 96-well plates and treated for 30 min at 37°C, 5% CO_2, with control (BM-medium), 2-deoxy-D-glucose (2-DG, 100mM, Sigma-Aldrich), Oligomycin (Oligo, 1 µM, Sigma-Aldrich), or combination 2-DG + Oligomycin (for this last condition 2-DG was added for 15 min and Oligo supplemented for the next 15 min). Puromycin (Puro, 10 µg/mL, Sigma-Aldrich) was added for the last 15 min. Cells were washed in cold PBS and stained with a combination of mouse Fc receptor blockade and fluorophore-conjugated antibodies against surface markers for 30 min at 4ºC in flow cytometry Buffer (PBS 1X, 5% FCS, 2mM EDTA). Intracellular staining against puromycin was performed with Foxp3/Transcription factor staining kit (eBioscience), using an anti-puromycin monoclonal antibody (12D10, 1:600, Sigma-Aldrich), as described in the flow cytometry section. Cell dependencies and capacities were obtained as previously described (18).

Metabolite and type I IFN analysis

To quantify ATP, polarized BMDMs were plated on a 6-well plate, washed with PBS without Ca^{2+} and Mg^{2+} and stored at -20ºC. Next, cells were thawed for 30 min on ice and lysed with 50μl/well of extraction buffer 6M guanidine-HC (Sigma-Aldrich, G3272), 100mM Tris/HCl pH7.8 (Sigma-Aldrich, B9755), 4mM EDTA (Sigma-Aldrich, ED2SS). Cell lysates were incubated on ice for 5 min, snap-frozen, and then incubated at 95ºC for 3 min. Lysates were centrifuged at max speed for 10 min at 4ºC and supernatant collected. Protein quantification was performed using the Bradford Protein Assay Kit (5000001, BioRad), according to the manufacturer’s instructions. A Luciferase-based ATP Determination Kit (Molecular Probes/ThermoFisher Scientific, catalogue nº A22066) was used according to the manufacturer’s instructions and ATP content was determined based on a concentration standard curve.

pH quantification of the supernatants of the polarized BMDMs was performed with pH strips (Sigma). One drop was applied on the strip and the yielded color code was compared with a standard scale provided by the manufacturer. Glucose and lactate quantification was performed using a Cedex Bio Analyzer 7100 (Roche).

IFN-α and IFN-β were assessed with the Mouse IFN 2-Plex Discovery Assay manufactured by Eve Technologies (Calgary, Canada) according to the manufacturer’s instructions.

RNA Isolation, cDNA reverse transcription, and Real-Time PCR

mRNA was prepared from $CD11b^+$ FACS-isolated myeloid cell populations using High Pure RNA Isolation kit (Roche). cDNA and relative quantification was performed as described previously (19). Briefly, reverse transcription was performed with random oligonucleotides (Invitrogen) using Moloney murine leukemia virus reverse transcriptase (Promega) for 1 h at 42°C. Relative quantification of specific cDNA was performed with power SYBR® Green

PCR master mix (ref:4367659; applied Biosystems™) on a ViiA™ 7 Real Time PCR system (applied biosystems™). The Ct values were calculated on QuantStudio ™Real-Time PCR Software v1.7.2 (applied biosystems™). Exported values of Ct for the target gene was subtracted from the Ct for endogenous reference gene (*β2 microglobulin*), and the relative amount was calculated as 2−ΔCT. Primer sequence: *b2m* fwd, CTCGGTGACCCTGGTCTTTC, b2m rev, GGATTTCAATGTGAGGCGGG, *cxcl9* fwd, CGAGGCACGATCCACTACAA, *cxcl9* rev, GAGTCCGGATCTAGGCAGGT.

Kaplan-Meier survival curves

Plots of survival curves for human patients were based on normalized gene expression data for 1,985 primary breast tumors from the Molecular Taxonomy of Breast Cancer International Consortium (METABRIC) (20) and respective metadata (including information on survival and hormone receptors), retrieved from European Genome-Phenome Archive (EGAC00001000484). In the data retrieved, gene expression profiling had been performed with Illumina HT-12 v3 microarrays, with probe-level intensity values being mean-summarized per gene. We determined relative TAM enrichment, for each tumor sample, by summing the relative abundances of M0, M1, and M2 macrophages, as estimated by CIBERSORTx (21) based on gene expression. Samples were divided into "TAM rich" and "TAM poor" based on the median value of that enrichment. For all plots, stratification of patients into "High" and "Low" was based on the median value of the classifying feature. Plots were generated in R (v. 4.3.1), running function autoplot, from package ggplot2 (v. 3.4.2) (22), on curves generated with functions Surv and survfit from package survival (v. 3.5-5) (23). Function survdiff, also from package survival, was used to test for the differences between the curves, with significance given by the p-value corresponding to the Chi-square statistic.

Statistical analysis

Statistics were done in GraphPad Prism v8.4.3 (GraphPad Software) using non-parametric two-tailed Mann-Whitney test. Unless otherwise indicated, individual values and mean are plotted or standard deviation. *$p < 0.05$; **$p < 0.01$; ***$p < 0.001$, ****$p < 0.0001$. Graphs show data from at least two independent experiments unless otherwise stated.

Data availability

The data generated in this study are available within the article and its supplementary data files. The raw scRNA-seq FASTQ files generated in this study were deposited in the NCBI Sequence Read Archive (SRA) under accession PRJNA1156755 and are publicly available. Additionally, raw Market Exchange Format (MEX) files as returned by Cell Ranger, for each individual sample, along with batch effect corrected count matrices in log2(counts+1) for both the full dataset and the macrophage subset, are accessible via the NCBI Gene Expression Omnibus (GEO) under accession GSE276345. Processed Seurat .rds objects, including count matrices, metadata and clustering analysis results, are hosted on Zenodo (https://zenodo.org/records/13122751). Any further information about the scRNA-seq dataset generated or analyzed in this study is available from the corresponding authors upon request. All analysis scripts used in this study are available on GitHub (https://github.com/DiseaseTranscriptomicsLab/MCT).

Results

MCT induces tumoricidal phenotype and activity in BMDMs

Tumoricidal M1 macrophages are typically induced *in vitro* by LPS, a pathogen-associated TLR4 ligand, and IFN-γ, which mimics "help" from activated T cells. However, the combination of LPS and IFN-γ exhibits high toxicity, causing fever and sterile septic shock, which limits its use *in vivo* (24). To mimic the collaborative effects of innate and adaptive immune signals, we tested a combination of polyI:C, a TLR3 ligand, with an agonist anti-CD40 on BMDMs (Fig. 1A). We first compared putative tumoricidal properties of BMDMs with a phenotype induced by MCT, with that of M0, M1 and M2 polarization phenotypes as references (Fig. 1B). Approximately 30% and 47% of MCT-BMDMs expressed the molecules associated with tumoricidal properties, TNF-α and iNOS, respectively. In contrast, approximately 95% and 93% of M1-BMDMs expressed these effector molecules, respectively. We also looked at the expression of molecules involved in cell–cell interaction and T-cell activation. MCT induced similar proportions of ICAM-1$^+$ and MHC-II$^+$ BMDMs as M1 polarization (42% *versus* 26% for MHC-II, and 74% *versus* 65% for ICAM-1, respectively). Additionally, MCT induced PD-L1 expression to a similar extent as M1 polarization (50% *versus* 67%), while PD-L2 was not induced, unlike in M2 and M1 polarizations (53% versus 19%, respectively).

We next examined if MCT-BMDMs could affect tumor cell survival. Mouse E0771 breast cancer cells, stained with CFSE, were co-cultured with BMDMs for 48h and then analyzed by flow cytometry, using the M0 condition for normalization (Fig. 1C). Both MCT-BMDMs and M1-BMDMs significantly impaired E0771 tumor cell survival, resulting in about 57% and 19% live cells, respectively. As we expected, M2-BMDMs had no impact on E0771 tumor cell numbers. Direct contact was not required for the effects of MCT- and M1-BMDMs as supernatants from MCT- and M1-BMDMs also reduced E0771 tumor cell viability to about 70% and 45%, respectively (Fig. 1D). The conditioning MCT medium, by itself, did not affect E0771 tumor cell viability (Supplementary Fig. S1A). Live dead staining with annexin V and 7-AAD (Supplementary Fig. S1B) confirmed that conditioned medium from MCT- and M1-BMDMs induced on average death of 23% and 26% E0771 tumor cells, respectively (Fig. 1E). Altogether, our data showed that MCT induced tumor-killing macrophages.

We noticed that the supernatants of the different induced BMDM phenotypes exhibited different colors, likely indicative of different metabolic activities. Further analysis revealed higher glucose and lower lactate concentrations, with higher medium pH in MCT-BMDMs (7.7 and 7.1 mmol/L, respectively, and pH 7.6) compared to M1-BMDMs (5.8 and 11.1 mmol/L, respectively, and pH 6.1) (Fig. 1F). Consequently, ATP content was higher in MCT-BMDM than in M1-BMDM (0.11 *versus* 0.04 uM/20ug protein respectively) (Fig. 1F). Using SCENITH, a flow cytometry–based method relying on protein synthesis, for profiling energy metabolism at single-cell resolution (18), we found that MCT-BMDMs displayed a similar energetic profile compared to M0 and M2-BMDMs, and that only M1-BMDMs exhibited lower mitochondrial dependence and higher glycolytic capacity (Fig. 1G). This metabolic distinction correlated with higher viability of MCT-BMDMs compared to M1-BMDMs, with on average 46% *versus* 21% live BMDMs post polarization, respectively (Fig. 1H). Overall, these data indicate that MCT effectively programs BMDMs to be tumoricidal together with higher viability, lower local lactate concentration, and lack of PD-L2 expression, when compared to their M1-BMDM counterparts, potentially reducing local immunosuppression.

Repetitive injections of MCT are necessary for macrophage-dependent tumor regression in vivo

We investigated whether MCT could reprogram TAMs and induce tumor regression *in vivo*. Mice received $1x10^6$ E0771 breast tumor cells orthotopically in the mammary fat pad. When tumors reached 50-100 mm³, mice were treated with MCT (Fig. 2A). MCT was administered i.t. every 3 days until tumor elimination or upon reaching a humane endpoint (1,000mm^3). In not-treated and single-agent (Poly:IC or anti-CD40 only) treated animals, tumors grew steadily over 3 days (T3/T0 ratio > 1), while MCT-treated tumors were stable or regressed within 3 days post-treatment (T3/T0 ratio ≤ 1) (Fig. 2B). To further validate the therapeutic efficacy of MCT, we tested this treatment in 4 additional tumor models, MC38, CT26, B16F10, and LKR, which represent various cancer types (colorectal, melanoma, and lung) from different genetic backgrounds, and observed similarly sustained tumor control (Supplementary Fig. S2A-D). The effect on tumor growth was rapid (within 3 days) for highly immunogenic cell lines (E0771 and MC38), while it was delayed (7 days) in low immunogenic cell lines (LKR, B16F10, and CT26). We then focused on the E0771 cell line and assessed if tumor size at the start of MCT was an important parameter governing treatment response rate. Indeed, regression was more effective for smaller tumors, with response rates >90% for tumors under 80 mm3, ~50% in the 80-100 mm^3 range, and <30% for larger than 100m^3 tumors (Fig. 2C). Complete tumor regression occurred in 70% of the animals that received 3 MCT injections, compared to 10% and 20% after 1 and 2 injections, respectively (Fig. 2D-E). This underscores the necessity of at least 3 consecutive injections to effectively halt tumor growth. The median survival of NT mice was about 30 days, while approximately 71% of mice receiving 3 MCT injections were alive 45 days post-treatment (Fig. 2F). To confirm the key role of macrophages in the MCT response, we used clodronate-containing liposomes, which induce macrophage apoptosis. The clodronate-containing liposomes induced approximately a threefold reduction in F4/80$^+$Ly6C$^-$ TAMs (Supplementary Fig. S3A-C). They were administered one day before and one day after MCT, followed by additional doses at T3 and T6, concurrently with MCT (Fig. 2G), and this abolished the antitumor effect of the treatment (Fig. 2H). These results indicate that macrophages play a crucial role early post-MCT as the primary immune cell subset exerting direct antitumor functions.

Single-cell RNA sequencing reveals MCT-activated TAMs linked to tumor regression in vivo

We next sought to delineate the antitumor TAM phenotype following MCT. We analyzed TAMs at 12h and 72h post-MCT to capture both the early dynamics and later stages of tumor regression (Supplementary Fig. S4A). For the 72h time point, we selected responders with a tumor size ratio (T3/T0) ≤ 1 (Supplementary Fig. S4B). To differentiate between protumor and antitumor inflammation originating from TAMs, we collected tumor-infiltrating myeloid cells from untreated mouse progressing tumors (PT, >500 mm^3) (Supplementary Fig. S4A-B). Myeloid cells were sorted using a permissive live $\text{CD45}^{+}\text{CD19}^{-}\text{CD3}^{-}\text{NK1.1}^{-}$ cell gating approach (Supplementary Fig. S4C).

Using 10X Genomics, we obtained quality-controlled profiles from 40,446 cells across the four conditions (NT, MCT-12h, MT-72h, PT). Ten tumor-associated subsets were identified based on marker genes (Supplementary Fig. S5A). Macrophages were the main population, expressing *Itgam*, *Csf1r*, *Fcgr1*, *Cd14*, *Adgre1*, *Cebpb*, *Fcgr3*, *Maf*, *Mafb*, and *Cd68*, and segregated into *Lyz2* #0Mac and *Nos2* #3Mac clusters (Supplementary Fig. S5A-B). Myeloid populations also included dendritic cells (DCs), identified by *Flt3*, *Batf3*, and *Cd83*. Subsets were monocyte-derived *Cd209a* #1cDC2 (*Cd209a*, *H2-dmb2*), conventional *Ccl22* #4cDC1 (*Ccl22*, *Ccr7*), and *Clec9a* #6cDC1 (*Clec9a*, *Xcr1*, *Itgae*), consistent with published datasets (9). Additionally, we identified *Siglech* #7 plasmacytoid DCs (*Siglech*, *Ccr9*, *Klk1*, *Tcf4*), and *Cpa3* #8 mast cells (*Cpa3*, *Gata2*, *Mrgprb2*, *Mcpt4*). Other clusters included CD8^{+} T cells, CD4^{+} T cells, and NK cells, identified within clusters #2 and #5 (*Cd3e*, *Cd8a*, *Cd4*, *Gzma*, *Gzmb*, *Prf1*), and *Col6a1* #9Fibroblasts (*Col6a1*, *Col3a1*, *Sparc*, *Aebp1*) (Supplementary Fig. S5A-B).

Myeloid subsets (clusters #0, #1, #3, #4, #6, #7, #8) were analyzed across conditions (Fig. 3A). Macrophages (clusters #0 and #3) dominated, constituting approximately 58–84% of myeloid cells, while DCs (clusters #1, #4 and #6) comprised approximately15–37% (Fig. 3A-B). WE observed that NT, MCT-72h, and PT were primarily composed of *Lyz2* #0Mac and *Cd209a* #1cDC2, whereas MCT-12h predominantly contained *Nos2* #3Mac and *Ccl22* #4cDC1.

Given the enrichment in *Ccl22* #4cDC1 at MCT-12h and their role in antitumor CD8^{+} T-cell responses, we assessed DCs in tumor control using *Batf3*$^{-/-}$ mice, which lack cDC1 (25, 26)**.** These mice, injected with E0771 cells followed by MCT, showed faster tumor growth in NT conditions (*T3/T0* ratio 1.25 in WT vs. 2 in *Batf3*$^{-/-}$, Fig. 2E vs. 3C), confirming the key role of cDC1 in antitumor immunity. Although MCT did not induce complete tumor eradication in *Batf3*$^{-/-}$ mice, it delayed tumor growth, particularly in the first 3 days post-treatment (Fig. 3C).

These data suggested that the initial antitumor effects of MCT, might be driven by the therapy-reprogrammed TAM compartment.

TAM clusters mainly segregate by condition

We next investigated which TAMs, *Lyz2* #0Mac or *Nos2* #3Mac, carried direct antitumor functions within the first 3 days post-MCT. Analyzing 23,453 cells, hierarchical clustering of pseudo-bulk RNA-seq data revealed two branches: one grouping MCT-12h and PT, and the other grouping MCT-72h with NT samples (Supplementary Fig. S6A). Unsupervised graph-based clustering of single-cell data yielded 9 clusters (Supplementary Fig. S6B), with the first 5 clusters comprising 86% of the cells (Supplementary Fig. S6C). Using published signatures (9, 27), we identified *Ly6c2* #1Mono as inflammatory classical monocytes and *Nr4a1* #4Mono and *Itgal* #7Mono as patrolling/non-classical monocytes (Supplementary Fig. S6D). The remaining clusters (#0, #2, #3, #5, #6, #8) were identified as macrophages. Hereafter, we will refer to macrophages as TAMs and monocytes as TAMonos. The distribution of these clusters across the four conditions (Fig. 4A) showed that TAMs from clusters #0, #1, #2, and #3 made up >40% of the total TAMs in NT, PT, MCT-72h, and MCT-12h, respectively, although cluster #1 monocytes were also present in PT (Fig. 4A-B). This distribution suggested dynamic changes in the TME, where stimuli like MCT or a progressing tumor influence macrophage phenotype and function.

TAM clusters in NT and PT tumors associate with selective TAM functions

We identified distinct TAM clusters in NT and PT tumors with specific functions. *C1qa* #0TAMs, predominantly found in NT tumors, expressed high levels of *C1qa/b/c*, *H2-Eb1*, *H2-Aa*, *H2-Ab1*, and *Apoe*, along with lower levels of *Trem2* and *Mrc1* (CD206) (Fig. 4C). These TAMs align with lipid-associated TAMs (LA-TAMs) (12), which are known for immunosuppressive functions (28, 29).

Cxcl10 #1TAMonos, present in PT and NT, were identified as inflammatory classical monocytes, and expressed *Ifit3*, *Isg15*, *Rsad2*, *Cxcl10* and tumor progression markers *Chil3* and *Vcan* (Fig. 4C). This cluster displayed various functional activities of ROS, IFN-α/βIFN-γ/inflammatory responses, allograft rejection, complement and TNF-α signaling pathways, along with protumor TGF-β response and angiogenesis (Fig. 4D, Supplementary Fig. S6E).

Spp1 #5TAMs, enriched in PT, expressed *Spp1*, *Arg1*, *Vegfa*, and *Hmox1* (Fig. 4C). This cluster lacked hallmarks associated with IFN-α/βIFN-γ responses, but displayed glycolysis, hypoxia and angiogenesis features (Fig. 4D, Supplementary Fig. S6E), and has been referred to as pro-angiogenic Angio-TAMs (9, 12).

S100a9/8 #6TAMs, have been proposed to belong to monocyte (30) or M-MDSC (31) subsets, but they lacked classical monocyte identity genes (*Fcn1*, *Fn1*, *Lyz2*, *Hp*, *Sell*) (Fig. 4C, Supplementary Fig. S6D), We categorized them as inflammatory/immunosuppressive macrophages, as previously proposed (32). *S100a9/8* #6TAMs showed the most diverse functionalities, displaying the greatest range of activities across hallmark pathways notably, the highest activity in TGF-β, estrogen early and late responses (Fig. 4D, Supplementary Fig. S6E), which are associated with robust immunosuppression (33) (Fig. 4D, Supplementary Fig. S6E). Consistent with their exclusive presence in PT, *S100a9/8* #6TAMs shared epithelial-mesenchymal transition (EMT), glycolysis, hypoxia and angiogenesis features with *Spp1* #5TAMs (Fig. 4D, Supplementary Fig. S6E). Unlike *Spp1* #5TAMs, *S100a9/8* #6TAMs exhibited high levels of inflammatory signatures. Revealing their duality, *S100a9/8* #6TAMs are enriched in both M1- or M2-associated genes (34) (Fig. 4E, Supplementary Fig. S6F).

We also observed three monocyte clusters: inflammatory classical monocytes *Cxcl10*+ #1TAMonos (in NT and PT), patrolling non-classical monocytes *Hp*+ #4TAMono, and *Nedd9*+ #7TAMono (Fig. 4C, Supplementary Fig. S6D). Given their broad distribution (Fig. 4B), these monocytes could differentiate into various TAM types, supporting the idea that *C1qa* #0TAMs and *Spp1* #5TAMs likely derive from tumor-infiltrating monocytes (9).

TAM clusters in MCT tumors show transient antitumor features

After MCT injection, TAMs displayed unique functional profiles. At 12h post-MCT, tumors were composed of approximately 80% of *Nos2* #3TAMs and, to a lesser extent, *C1qa* #0TAMs, *Nedd9* #7TAMono, and *Ccr7* #8TAMs. *Nos2* #3TAMs and *Ccr7* #8TAMs did not clearly match any previously published signatures, indicating that they differed from TAMs seen in progressing tumors or those induced by CSF1R blockade or anti-CD40 treatment (Supplementary Fig. S6D) (9, 27)(9). *Nos2* #3TAMs were characterized by the expression of *Ccl5*, *Nos2*, *Slc7a2*, *Slc7a11*, *Prdx5* and *Dhfr* genes (Fig. 4C). Additionally, they co-expressed

Cd38, *Bst1* and *Bst2*, which are all members of the ADP-ribosyl cyclase family and catalyze the synthesis and hydrolysis of cyclic ADP-ribose. Through analysis of previously published data, we found that *Bst2* was associated with increased survival in patients with breast cancer (Supplementary Fig. S6G), while *Bst1* and *Ccl5* were associated with survival in patients with triple-negative breast cancer (TNBC) (Supplementary Fig. S6H) in a TAM-enriched manner. *Nos2* #3TAMs displayed activities of ROS, IFN-α/IFN-γ responses, allograft rejection, inflammatory response, complement and TNF-α signaling pathways (Fig. 4D, Supplementary Fig. S6E). Moreover, these *Nos2* #3TAMs expressed lower levels of immunosuppressive genes or hallmark pathways, compared to *Spp1* #5TAMs and *S100a9/8* #6 TAMs (Fig. 4D, Supplementary Fig. S6F), and we classified them as antitumor subsets. *Ccr7* #8TAMs expressed high levels of *Ccr7*, *Ccl22*, *Fscn1*, *Stat4* and *Il12b*, suggesting that they act as migratory Th1-inducer TAMs (Fig. 4C-D). Overall, MCT-12h resulted in the unique accumulation of specific TAMs with pro-inflammatory and antitumor properties.

By contrast, at 72h post-MCT, tumors were composed of approximately 58% of *Cxcl9* #2TAMs, followed by *Hp* #4TAMono, *C1qa* #0TAMs and to a lesser extent *Cxcl10* #1TAMono and *Spp1* #5TAMs (Fig. 4B). *Cxcl9* #2 TAMs showed high expression of *Cxcl9*, an antitumor cytokine induced by IFN-γ that recruits CXCR3-expressing T and NK cells (35), along with *Kcnn4*, and *Pf4* (CXCL4) (Fig. 4C), which have been associated with protumor functions. *Cxcl9* #2TAMs mainly displayed high Myc targets pathway activities. The Myc gene family and its products promote cell proliferation, immortalization, dedifferentiation, and transformation, suggesting that *Cxcl9* #2TAMs or their precursors had undergone a recent adaptive change, possibly reflecting a shift towards a more pro-tumorigenic phenotype. This aligns with the proposed role of MYC in macrophages to limit glycolysis and reduce the production of inflammatory cytokines (36)., While *Nos2* #3TAMs were enriched in M1 genes, they were also the cluster with the lowest expression of M2 genes (Fig. 4E, Supplementary Fig. S6F). Conversely, *Cxcl9* #2TAMs exhibited the lowest expression of M1 genes but displayed high expression of M2 genes (Fig. 4E, Supplementary Fig. S6F).

When compared to *Nos2* #3TAMs, *Cxcl9* #2TAMs were characterized by Myc target and oxidative phosphorylation (Supplementary Fig. S6I). This was consistent with *Cxcl9* #2TAMs expressing high levels of mitochondria-associated genes such as *mt-Nd3*, *mt-Cytb*, *mt-Co2*

(Fig. 4C), suggesting an involvement in mitochondria biogenesis. *Nos2* #3TAMs displayed a more active glycolytic metabolism (Fig.4E, Supplementary Fig. S6F), whereas *Cxcl9* #2TAMs upregulated genes belonging to the 5 complexes of the electron transport chain, indicating mitochondrial activity (Fig.4E, Supplementary Fig.S6F). Taken together, these results suggest that TAMs were equipped with antitumor properties by 12h post-MCT but were unable to sustain these antitumor functions, as visualized at 72h post-MCT by the disappearance of *Nos2* #3TAMs and the appearance of *Cxcl9* #2TAMs, which accumulated tumor-promoting features and displayed different metabolic responses.

Antitumor inflammation is a hallmark of MCT and distinct from protumor inflammation

To define the specific characteristics of the antitumor *Nos2* #3TAMs, we compared them with the pro-inflammatory TAMs that accumulated in the NT and PT conditions, namely *C1qa* #0TAMs, *Cxcl10* #1TAMono and *S100a9/8* #6TAMs (Supplementary Fig. S6I-L). *Nos2* #3TAMs exhibited heightened antitumoral pathways than the *C1qa* #0TAMs (Supplementary Fig. S6J). By contrast, *Nos2* #3TAMs shared IFNα/γ pathways with *Cxcl10* #1TAMono and *S100a9/8* #6TAMs (Fig. 4D, Supplementary Figs. S6E and S6K). To discern differences between *Nos2* #3TAMs and those two subsets, we analyzed the leading-edge genes that contributed to the upregulation of inflammatory pathways in each cluster relatively to the remaining macrophages. This approach revealed distinct leading-edge genes for IFNα/γ pathways between *Nos2* #3TAMs and *Cxcl10* #1TAMono, for example excluding *Cxcl9* and *Cxcl10* between the two subsets in the IFN-γ pathways (Supplementary Fig. S6M). This is consistent with *Cxcl9*, but not *Cxcl10*, being associated with increased survival in patients with TNBC in a TAM-enriched manner (Supplementary Fig. S6H). Similarly, *Nos2* #3TAMs uniquely expressed genes involved in MHC protein binding and antigen presentation (*B2m, Tap1, Psme2, Psmb9, Psme1, Psmb8, Psma3, Psmb2, H2-Q7*) for IFNα/γ pathways distinguishing them from *S100a9/8* #6TAMs (Supplementary Fig. S6N). This suggests that *Nos2* #3TAMs were likely better equipped to interact with and activate T cells in the post-MCT TME. Consistently, *Nos2* #3TAMs and *Ccr7* #8TAMs displayed a higher score for lymphocyte activation signature, whereas *S100a9/8+* #6TAMs scored high for myeloid activation signature (Fig.4E, Supplementary Fig. Fig. S6F). *Nos2* #3TAMs shared the expression of genes involved in antigen processing and presentation with *C1qa* #0TAMs, *Cxcl10* #1TAMono, *S100a9/8*+ #6TAMs and *Ccr7* #8TAMs (Fig.4E, Supplementary Fig.S6F).

Moreover, *Nos2* #3TAMs shared the TNF-α pathway with *S100a9/8* #6TAMs (Fig. 4D, Supplementary Fig. S6E). The leading-edge genes expressed by *S100a9/8* #6TAMs uniquely highlighted the IL-17 signaling pathway that comprises genes involved in myeloid recruitment (*Il1b, Ccl2, Ccl4, Ccl7, Cxcl2, Cxcl3, Nfkb1, Ptgs2, Jun, Irak2*, besides *S100a8* and *S100a9*) a feature absent from *Nos2* #3TAMs (Supplementary Fig. S6O). This underscored the multifaceted role of TNF-α in the TME. Under certain circumstances, TNF-α can induce IL-17, a cytokine known to promote angiogenesis, enhance tumor cell survival and proliferation, and modulate the antitumor response (37). Altogether, this supports the idea that the antitumor functions of *Nos2* #3TAMs in part lies on their properties to foster a TME favorable to T-cell recruitment and activation.

Protective processes against oxidative stress specifically characterize antitumor MCT TAMs

Some of the most differentially expressed genes in *Nos2* #3TAMs were associated with oxidative stress, including nitric oxide (NO) metabolism (*Nos2, Slc7a2, Slc7a11 and Dhfr*) (Fig. 4C). *Slc7a2* mediates the cellular uptake of arginine, a substrate for iNOS responsible for NO production. Dihydrofolate reductase (*Dhfr*) was also found to participate in NO bioavailability (38). Increased NO production is proposed to lead to augmented ROS and therefore to enhanced cytotoxic function (39). This aligns with *Slc7a11*, which imports cystine, the precursor of glutathione, that acts as a co-factor for enzymes responsible for scavenging ROS. We thus assessed whether genes encoding enzymes involved in antioxidant processes, such as those maintaining the reduced state of glutathione (GSH), detoxifying ROS with reduced glutathione, and scavenging hydrogen peroxide, would be specifically expressed by *Nos2* #3TAMs. Indeed, *Nos2* #3TAMs expressed a higher signature of cell defense against oxidative stress (Fig.4E, Supplementary Fig. S6F).

To validate this signature, we measured intracellular GSH by flow cytometry. GSH neutralizes ROS by acting as an electron donor, directly reducing oxidative stress within cells. Thus, it serves as a key indicator of a cell's ability to defend itself against oxidative damage. We found that TAMs harvested from tumor-bearing mice treated with MCT (24h or 72h earlier) displayed significantly higher GSH levels compared to TAMs from NT animals

(Supplementary Fig. S7A-B). This result indicated that the increased oxidative stress protection gene signature in *Nos2* #3 TAMs was associated with elevated GSH levels, highlighting an intrinsic mechanism of self-protection against oxidative stress. Altogether, these results suggest that the production of NO and ROS could be participating in the antitumor mechanisms by which *Nos2* #3TAMs control tumor growth.

Secondary MCT injection boosts expression of iNOS, TNF-α and CD38 in TAMs

Next, we sought to validate the findings of the scRNA-seq data at the protein level, particularly the hypothesis that prolonged stimulation is required for TAMs to maintain their antitumor phenotype. Thus, we used flow cytometry to investigate whether two consecutive MCT injections could sustain specific local antitumor phenotypes and functions of TAMs. Tumor-bearing mice were either left untreated or administered MCT either once or twice with a 3-day interval (Fig. 5A). Tumor samples were collected at 24h, 3 days and 4 days post-MCT, some mice having received one injection (D4 1x) and others two (D4 2x). We collectively gated on myeloid cells identified as CD3e^{-}CD19^{-}NK1.1^{-} cells, successively excluding CD11c^{-}CD11b^{-} double-negative cells, then Ly6G^{+} cells, and finally Ly6C^{-}F4/80^{-} double-negative cells (TAMs + TAMonos) (Supplementary Fig. S8A). We evaluated the expression levels of iNOS, TNF-α, CD38 and MHC-II, identified as specific markers of the *Nos2* #3TAMs (Fig. 4C, Supplementary Fig. S8A). MCT increased the proportion of iNOS^{+}, TNF-α^{+}, CD38^{+} and MHC-II^{+} cells among TAMs + TAMonos as early as one day post-injection (Fig. 5B). By D3 (and D4 x1) post-MCT, the proportions of iNOS^{+}, CD38^{+}, and MHC-II^{+} TAMs + TAMmonos decreased compared to D1, while TNF-α^{+} cells were maintained. A second MCT injection boosted the proportions of iNOS^{+} and CD38^{+} cells, increasing their levels between D4 x1 and D4 x2. MHC-II^{+} expressing TAMs+ TAMmonos were not significantly affected by the second injection (Fig. 5B). Altogether, the comparison of TAM responses after one or two injections showed that maintenance of antitumor TAMs required regular local reprogramming.

ROS and TNF-α are potent antitumor effector mechanisms of TAMs early after MCT injection

The elevated expression of genes involved in detoxifying ROS, along with glutathione-precursor transporter (*Slc7a11*) expression (Fig. 4C, Supplementary Fig. S6F), suggested that

MCT-responding TAMs were actively producing and protecting themselves against ROS. Furthermore, the confirmation of iNOS and TNF-α protein production by TAMs *in vivo* in response to MCT (Fig. 5B, Supplementary Fig. S8A) prompted an assessment of their antitumor role. Tumor-bearing mice received systemic and intratumoral injections of the antioxidant NAC or iNOS inhibitors or blocking anti-TNF-α (Supplementary Fig. S8B). Despite using a combination of two known iNOS inhibitors (1400W, aminoguanidine hydrochloride), MCT effectively prevented tumor growth (Fig. 5C). To further validate these data, *Nos2*$^{-/-}$ mice received E0771 tumor cells followed by MCT. Consistent with the lack of effect of the iNOS inhibitors, MCT effectively induced tumor eradication in *Nos2*$^{-/-}$ mice, and limited tumor growth as early as 3 days post treatment (Supplementary Fig. S8C). This suggested that iNOS and NO production were not involved in the antitumor properties of MCT-TAMs. By contrast, antioxidant NAC (Fig. 5D) and the blocking TNF-α antibody (Fig. 5E) partially inhibited the effect of MCT while showing no impact in MCT-untreated tumors. NAC is a potent antioxidant that works by replenishing intracellular levels of GSH, as it serves as a precursor to cysteine, a key amino acid required for glutathione synthesis. *Nos2* #3TAMs are likely controlling tumor growth through high production of ROS. These ROS have the properties to damage tumor cells directly by causing oxidative stress, which can lead to apoptosis or inhibit tumor cell proliferation. By reducing ROS levels, NAC impairs the antitumor effector functions of the *Nos2* #3TAMs. This demonstrated the importance of ROS and TNF-α in MCT-induced antitumor effector functions.

MCT-TAMs enhance tumor self-antigenic complexes via an IFN-α/β-dependent mechanism

IFNα/γ pathways were present in *Nos2* #3TAMs, *Nedd9* #7TAMono and *Ccr7* #8TAMs which represent over 90% of the TAMs within the MCT-12h tumors (Fig. 4B), whereas they were absent from the MCT-72h TAMs (Fig. 4D, Supplementary Fig. S6E). The IFNα/γ pathways were also expressed in *C1qa* #0TAMs, *Cxcl10* #1TAMono, *S100a9/8+* #6TAMs (Fig. 4D, Supplementary Fig. S6E), which represent about 70% and 65% of the TAMs in NT and PT tumors, respectively (Fig. 4B). Given the antitumor functions of type I and II IFNs, we sought to determine whether MCT-BMDMs could secrete IFN-α/β. Both M1- and MCT-BMDMs secreted IFN-α and IFN-β, unlike M0- and M2a-BMDMs (Fig. 6A). Moreover, the concentration of IFN-β was over tenfold higher than that of IFN-α. We then investigated whether IFN-α/β could boost tumor cell immunogenicity. Ovalbumin-expressing E0771

(OVA-E0771) cells and control cells transfected with an empty GFP-vector (GFP-E0771) were incubated overnight with supernatants of M0-, M1-, M2-, or MCT-BMDMs. The supernatants of MCT- and M1-BMDMs induced upregulation of H-2Kb molecules on both GFP- and OVA-E0771 cells (Fig. 6B – left graphs). As we expected, tumor self-antigenic complex expression, assessed by the generation of OVA-derived peptide – SIINFEKL – complexed with H-2Kb molecules, was only up-regulated on OVA-E0771 cells by the supernatants of MCT- and M1-BMDMs (Fig. 6B – right graphs). The conditioning MCT-polarization medium (PolyI:C and anti-CD40) had no impact on expression of H-2Kb-SIINFEKL complexes, whereas M1-polarization medium (IFN–γ and LPS) medium alone induced expression of these complexes (Supplementary Fig. S9A).

This suggested that MCT-BMDMs produced IFN type I responsible for the expression of self-antigen MHC complexes by tumor cells. Blocking IFN-α/β receptor (IFN-α-R) abolished the effect of MCT-BMDM supernatant, whereas blocking IFN-γ or TNF-α did not impair up-regulation of H-2Kb-SIIN complexes by OVA-E0771 cells (Fig. 6C). Anti-IFN-α-R or anti-IFN-γ failed to prevent self-presentation by tumor cells in the presence of M1-BMDM supernatant, likely due to redundant effects of these cytokines (with IFN-γ being part of the polarizing M1-condition). Thus, MCT-induced TAMs may also contribute to tumor eradication by inducing local production of IFN-α/β and thereby sensitizing tumor cells to $CD8^+$ T-cell recognition *in vivo*.

MCT induces intratumoral accumulation of $CD8^+$ T cells, which are required for long-term tumor eradication

One of the top differentially expressed genes in TAMs at 72h was *Cxcl9*, an antitumor chemokine known to recruit cytotoxic $CD8^+$ T cells (*Cxcl9* #2TAMs, Fig. 4C, Supplementary Fig. S9B). We examined the kinetics of *Cxcl9* mRNA expression by RT-PCR on $CD45^+CD11b^+CD3e^-CD19^-NK1.1^-Ly6G^-$ cells, from tumor samples collected from NT, or 1, 3, 4 and 7 days post-MCT animals. *Cxcl9* mRNA levels steadily increased after one (day 3), two (day 4) and three (day 7) MCT administrations (Fig. 6D).

The essential role of T cells in long-term tumor eradication was underscored by MCT administration in tumor-bearing $Rag2^{-/-}\gamma c^{-/-}$ or $Tcr\alpha^{-/-}$ mice (Fig. 6E). In the absence of conventional αβ T cells, MCT-stimulated TAMs induced only tumor growth delay (T3/T0 ratio lower than NT but close to 2), failing to stop tumor growth. By contrast, γδ T cells ($Tcr\delta^{-/-}$), NK cells ($Il15r^{-/-}$ or depleted using the anti-NK1.1 antibody) and B cells ($Jht^{-/-}$) were dispensable for MCT efficacy (Supplementary Fig. S9C). Then, we evaluated the kinetics of the T-cell response post-MCT. Tumor samples were collected from NT or 3 days and 7 days post-MCT. We focused on CD8$^+$ T cells, which we gated as CD45$^+$CD8$^+$CD11b$^-$ cells, and quantified effector CD8$^+$ T cells based on IFN-γ production (Supplementary Fig. S9D). Effector IFN-γ-producing CD8$^+$ T cells increased from about 8% in NT tumors to 21% at 3 days and up to 40% at 7 days post-MCT (Fig .6F). Depletion of CD8$^+$ T cells (Supplementary Fig. S9E) did not impair early (day 3) but inhibited late (day 7) MCT effects (Fig. 6G). Moreover, MCT-treated mice were resistant to rechallenge on the contralateral mammary fat pad as late as 50 days post-primary inoculation of E0771 cells, suggesting that MCT induced an effective memory response (Fig. 6H). Collectively, these findings suggest that MCT relies on macrophages as key innate effectors in the early antitumor response, setting the stage for adaptive CD8$^+$ T cells to enable long-term tumor control.

Discussion

TAMs play critical roles in tumor progression but can also contribute to antitumor immunity. To date, most macrophage-targeted strategies have focused on the blockade of CSF-1/CSF1R-signalling, which regulates macrophage differentiation and survival, or the CCL2/CCR2 axis, which regulates monocyte recruitment. *In situ* TAM reprogramming (40), although benefiting from diverse options for TLR agonists (41), presents the challenge of inducing protective inflammation rather than its more often associated protumor inflammation (42). Consequently, although macrophage-targeted therapy holds much promise, it has not yet reached the standard of care in the clinic as T lymphocyte–targeted therapies have, in the form of immune checkpoint blockers (ICB) or CAR T cells.

The omics era has exposed the extensive heterogeneity among TAMs in human cancers (9, 43). scRNA-seq experiments have revealed distinct TAM subsets, and different approaches have been proposed to categorize the diverse single-cell clusters based on highly upregulated genes and combining information regarding their function (11, 12, 44, 45) or by integrating various public data sets (27, 30). These efforts are crucial to allow the community to standardize the data across studies. However, somewhat surprisingly, there is a lack of description of clear antitumor clusters of TAMs, which represents a limitation overcome by our study.

Most of the TAM subsets that display pro-inflammatory features show an increased IFN-stimulated gene (ISG) signature, which is also associated with an elevated expression of protumor or immunosuppressive functions. Based on the nomenclature proposed by Ma *et al.*, tumor-infiltrating monocytes and macrophages, including IFN-TAMs, Inflam-TAMs, Reg-TAMs and LA-TAMs, all show local signs of response to IFN-γ concomitantly associated with cancer cell motility and suppression of adaptive immunity (12). Our *Nos2* #3TAMs resemble IFN-TAMs as well as IL4l1_Mac(#6) cells from the MoMac-VERSE (30). They share with them several differentially expressed genes, including *Cd38*, *Cxcl9*, *ISG20*, although *Nos2* appears unique to *Nos2* #3TAMs. Conversely, they lack expression of *Ido1/2* or *IL4l1* suggesting that *Nos2* #3TAMs do not promote local tryptophan degradation that may in turn suppress T cells and attract Treg cells into the tumor (46). Moreover, *Nos2* #3TAMs are also closest to the macrophages harvested from inflamed tissues (colitis and lupus nephritis patients) that display specific pathways related to oxidative phosphorylation and cellular stress (30). Our data suggest that the absence of protumor features in the macrophage compartment may be a critical determinant impairing cancer progression as supported by the recent study revealing that macrophage polarity, defined by CXCL9 and SPP1 expression, had a strong prognostic association (47).

We noticed that within *Nos2* #3TAMs most TAMs expressed C*cl5, Nos2, Slc7a2, Slc7a11, CD38, H2-q6, Prdx5, Dhfr, Bst1* and *Bst2*. We confirmed the specific expression of iNOS and CD38 in this population. Although the relevance of iNOS for tumor killing has long been recognized both *in vitro* and *in vivo* (48), we did not demonstrate that iNOS is a key antitumor factor in our system. Nevertheless, it is likely being responsible for local production of NO, which can alter the TCA cycle and reroute pyruvate away from mitochondrial metabolism, encouraging glycolysis, and orchestrating macrophage metabolic rewiring towards an inflammatory phenotype (49) in *Nos2* #3TAMs (MCT-12h), but not in *Cxcl9* #2TAMs (MCT-72h). This is consistent with iNOS being expressed in a higher proportion of TAMs at day 1 compared to day 3 post-MCT. Notwithstanding, iNOS remains, along with CD38, a biomarker of antitumor features of TAMs.

Our findings further identified that *Nos2* #3TAMs likely carry diverse antitumor functions, with pivotal roles for ROS and TNF-α as potent *in vivo* antitumor effector molecules. Both molecules are known to have dual roles. ROS mediate key macrophage functions such as phagocytosis, antigen presentation and recognition, cytolysis, and phenotypic differentiation. However, under certain circumstances, they can exert immunosuppressive effects on T cells (50). TNF-α is a critical cytokine capable of blocking protumoral gene expression in TAMs (51) and enhancing $CD8^+$ T-cell antitumor responses (52), but it can also foster cancer-promoting type of inflammation (53). Although both ROS and TNF-α signaling have complex activities in the TME, we hypothesize that, at early time points of tumor progression, they are beneficial. In addition, MCT-TAMs enhanced tumor immunogenicity and self-antigen presentation via an IFN-α/β-dependent mechanism. MCT induced the expression of *Ccl5* by *Nos2* #3TAMs and *Cxcl9* by *Cxcl9* #2TAMs, which in turn can participate in the accumulation of effector $CD8^+$ T cells that were responsible for tumor eradication and long-term protection. To date, the description of efficient antitumor macrophages is lacking as few other studies have performed scRNA-seq on tumor-infiltrating myeloid cells after administration of reprogramming agents. In the model of B16F10 melanoma, systemic treatment with TLR3 agonist was associated with a type-1 interferon signature, increased *Ccl5*, and macrophage antigen presentation gene expression (10). More data are needed to further understand the distribution and local impact of antitumour macrophages, such as *Nos2* #3TAMs, on tumors and T cells and their capacity to reshape the TME.

In large tumors, the TME undergoes discrete steps that contribute to tumor progression, such as the "angiogenic switch" (54), local production of tumor survival factors, and strong immunosuppression, likely limiting the impact of MCT. Angio-TAMs, which accumulate in PT, are resistant to therapeutic treatment with anti-CSF1R blockade (9) and likely insensitive to MCT. The composition of TAMs in the tumor is a probable determinant of the response to MCT. In early NT tumors, the TME is mainly constituted by *C1qa* #0TAMs and *Cxcl10* #1TAMono, which are potentially capable of being converted into *Nos2* #3 TAM. The protective *Nos2* #3TAMs were identified at 12h post-MCT but were replaced by *Cxcl9*

#2TAMs by 72h post-MCT, suggesting that this subset failed to be sustained in TME. Our work identifies a therapeutic vulnerability and proposes a better strategy to sustain antitumor TAMs. Indeed, the TME 72h post-MCT is permissive to generation of new iNOS$^+$ CD38$^+$ TAMs upon new administration of MCT. Only repetitive MCT injections would support a TME capable of maintaining *Nos2* #3TAMs. It is plausible that, once the local T cell response is ongoing, there is a positive feedback loop between intratumoral effector T cells and TAMs. The IFN-γ produced by T cells polarizes *Nos2* #3TAMs, which, in turn, reshape the TME to facilitate T-cell infiltration, immune function, and tumor rejection (31, 55). This is consistent with our hypothesis that macrophages have the potential to boost every step of the cancer–immunity cycle (41).

While ICBs have revolutionized the treatment of solid cancers, most patients fail to benefit from this immunotherapy due to primary and acquired drug resistance. ICOS co-stimulation and anti-CTLA-4 blockade therapy profoundly remodeled both lymphoid and myeloid compartments (55). The crosstalk between antitumor TAM and cytotoxic T cells has been shown critical to create a positive loop that supports effective immunotherapy to promote tumor control (31). Thus, the adaptability of TAMs to respond to therapies should be considered during tumor treatment(s). Moreover, simultaneous targeting of TAMs to enhance the efficacy of certain therapies (56), for instance, is a combination strategy to enhance antitumor immunity of irradiation or CAR T cells, (57, 58). In this context, our results should accelerate translational research as they advocate for a strategy based on *in situ* repeated reprogramming of macrophages. The new era of single-cell transcriptomics and subsequent integration of various datasets and information will pave the way to help the scientific community to advance innovative and more specific macrophage-based immunotherapy strategies.

Limitation of the study

We have used an orthotopic breast cancer mouse model in this study, and this may explain why we failed to identify tissue-resident macrophages (typically expressing *Lyve1*, *Retnla*, *Marco*, *Folr2*, *Hes1*) (59, 60) or proliferating macrophages (typically expressing *mki67*, *Top2a*, *Tubb*, *Tuba1b*). This suggests that our mouse model of implanted syngeneic E0771 tumor cell line primarily recruited monocyte-derived macrophages. This aligns with the heterogeneity within the *Nos2* #3TAMs and the clear segregation of the antitumor functions concentrated in one sub-cluster, while the other displayed a monocyte-signature. Although monocyte-derived TAMs are the most prominent (61, 62) and TAMs predominantly manifest monocyte-derived phenotypic features in trajectory analysis (63, 64), orthotopic models failed to recapitulate a role for tissue-resident macrophages (65). It will thus be important to determine the impact of reprogramming-type treatments on tissue-resident macrophage-derived TAM in spontaneous tumor mouse models.

Acknowledgments: We are grateful to the staff of the Flow Cytometry and Bioimaging Platforms as well as Animal Facilities of Instituto de Medicina MolecularJoão Lobo Antunes (iMM-JLA) Lisboa and to the staff of Genomics Facility from Instituto Gulbenkian de Ciência (IGC) Oeiras, for the valuable technical assistance and helpful discussions. We thank Caetano Reis e Sousa (Crick Institute, London, UK), Luis Graça (iMM-JLA) and Mark Veldhoen (iMM-JLA) for providing key mouse models and depletion antibodies. We thank Jocelyne Demengeot and Catarina Moita who provided the OVA-GFP plasmid. The authors acknowledge the parsimonious use of AI, specifically for text shortening and editing assistance. We want to thank deeply Julie Darrigues, Ângelo Chora and Pedro Papotto for captivating scientific discussions, and all the Ribot_Silva-Santos' lab for the professional, efficient and also joyful work environment!

Author contributions: C.J., M.B., M.R.S., A.T.M., K.S., performed most experiments and analyzed the data; E.P.L., H.B., H.K., M.R., N.G-S., N.S., S.M., T.S., and V.M. helped performing experiments and/or analyze data, and participated in result discussions and critical suggestions; M.P. and R.L. obtained the preliminary data that initiated this study; R.A. provided scientific support and reagents for SCENITH™ protocol and contributed to fruitful discussions; K.S., designed experiments and wrote the manuscript; K.S., B.S.S. and N.L.B.-M. supervised the study.

References

1. Cassetta, L., and J. W. Pollard. 2023. A timeline of tumour-associated macrophage biology. *Nat. Rev. Cancer* 23: 238–257.
2. Zhang, Q., L. Liu, C. Gong, H. Shi, Y. Zeng, and X. Wang. 2012. Prognostic Significance of Tumor-Associated Macrophages in Solid Tumor : A Meta-Analysis of the Literature. *PLoS One* 7.
3. Bingle, L., N. J. Brown, and C. E. Lewis. 2002. The role of tumour-associated macrophages in tumour progression: Implications for new anticancer therapies. *J. Pathol.* 196: 254–265.
4. Honkanen, T. J., A. Tikkanen, P. Karihtala, M. Mäkinen, J. P. Väyrynen, and J. P. Koivunen. 2019. Prognostic and predictive role of tumour-associated macrophages in HER2 positive breast cancer. *Sci. Rep.* 9: 1–9.
5. Macciò, A., G. Gramignano, M. C. Cherchi, L. Tanca, L. Melis, and C. Madeddu. 2020. Role of M1-polarized tumor-associated macrophages in the prognosis of advanced ovarian cancer patients. *Sci. Rep.* 10: 1–8.
6. Bruni, D., H. K. Angell, and J. Galon. 2020. The immune contexture and Immunoscore in cancer prognosis and therapeutic efficacy. *Nat. Rev. Cancer* 20: 662–680.
7. Murray, P. J., J. E. Allen, S. K. Biswas, E. A. Fisher, D. W. Gilroy, S. Goerdt, S. Gordon, J. A. Hamilton, L. B. Ivashkiv, T. Lawrence, M. Locati, A. Mantovani, F. O. Martinez, J. L. Mege, D. M. Mosser, G. Natoli, J. P. Saeij, J. L. Schultze, K. A. Shirey, A. Sica, J. Suttles, I. Udalova, J. A. vanGinderachter, S. N. Vogel, and T. A. Wynn. 2014. Macrophage Activation and Polarization: Nomenclature and Experimental Guidelines. *Immunity* 41: 14–20.
8. Azizi, E., A. J. Carr, G. Plitas, A. E. Cornish, C. Konopacki, S. Prabhakaran, J. Nainys, K. Wu, V. Kiseliovas, M. Setty, K. Choi, R. M. Fromme, P. Dao, P. T. McKenney, R. C. Wasti, K. Kadaveru, L. Mazutis, A. Y. Rudensky, and D. Pe'er. 2018. Single-Cell Map of Diverse Immune Phenotypes in the Breast Tumor Microenvironment. *Cell* 174: 1293-1308.e36.
9. Zhang, L., Z. Li, K. M. Skrzypczynska, Q. Fang, W. Zhang, S. A. O'Brien, Y. He, L. Wang, Q. Zhang, A. Kim, R. Gao, J. Orf, T. Wang, D. Sawant, J. Kang, D. Bhatt, D. Lu, C. M. Li, A. S. Rapaport, K. Perez, Y. Ye, S. Wang, X. Hu, X. Ren, W. Ouyang, Z. Shen, J. G. Egen, Z. Zhang, and X. Yu. 2020. Single-Cell Analyses Inform Mechanisms of Myeloid-Targeted Therapies in Colon Cancer. *Cell* 181: 442-459.e29.
10. Thomas, G., L. Micci, W. Yang, J. Katakowski, C. Oderup, P. Sundar, X. Wang, K. G. Geles, S. Potluri, and S. Salek-Ardakani. 2021. Intra-Tumoral Activation of Endosomal TLR Pathways Reveals a Distinct Role for TLR3 Agonist Dependent Type-1 Interferons in Shaping the Tumor Immune Microenvironment. *Front. Oncol.* 11: 1–10.
11. Wang, J., N. Zhu, X. Su, Y. Gao, and R. Yang. 2023. Novel tumor-associated macrophage populations and subpopulations by single cell RNA sequencing. *Front. Immunol.* 14: 1–13.
12. Ma, R. Y., A. Black, and B. Z. Qian. 2022. Macrophage diversity in cancer revisited in the era of single-cell omics. *Trends Immunol.* 43: 546–563.
13. Nalio Ramos, R., Y. Missolo-Koussou, Y. Gerber-Ferder, C. P. Bromley, M. Bugatti, N. G. Núñez, J. Tosello Boari, W. Richer, L. Menger, J. Denizeau, C. Sedlik, P. Caudana, F. Kotsias, L. L. Niborski, S. Viel, M. Bohec, S. Lameiras, S. Baulande, L. Lesage, A. Nicolas, D. Meseure, A. Vincent-Salomon, F. Reyal, C. A. Dutertre, F. Ginhoux, L. Vimeux, E. Donnadieu, B. Buttard, J. Galon, S. Zelenay, W. Vermi, P. Guermonprez, E. Piaggio, and J. Helft. 2022. Tissue-resident FOLR2+ macrophages associate with CD8+ T cell infiltration in human breast cancer. *Cell* 185: 1189-1207.e25.
14. Joshi, S., L. López, L. G. Morosi, R. Amadio, M. Pachauri, M. Bestagno, I. P. Ogar, M. Giacca, G. M. Piperno, D. Vorselen, and F. Benvenuti. 2024. Tim4 enables large peritoneal macrophages to cross-present tumor antigens at early stages of tumorigenesis. *Cell Rep.* 43.
15. Almeida-Santos, J., M.-L. Bergman, I. A. Cabral, and J. Demengeot. 2021. Interruption of Thymic Activity in Adult Mice Improves Responses to Tumor Immunotherapy. *J. Immunol.* 206: 978–986.
16. Lopes, N., C. McIntyre, S. Martin, M. Raverdeau, N. Sumaria, A. C. Kohlgruber, G. J. Fiala, L. Z. Agudelo, L. Dyck, H. Kane, A. Douglas, S. Cunningham, H. Prendeville, R. Loftus, C. Carmody, P. Pierre, M. Kellis, M. Brenner, R. J. Argüello, B. Silva-Santos, D. J. Pennington, and L. Lynch. 2021. Distinct metabolic programs established in the thymus control effector functions of γδ T cell subsets in tumor microenvironments. *Nat. Immunol.* 22: 179–192.
17. Subramanian, A., P. Tamayo, V. K. Mootha, S. Mukherjee, B. L. Ebert, M. A. Gillette, A. Paulovich, S. L. Pomeroy, T. R. Golub, E. S. Lander, and J. P. Mesirov. 2005. Gene set enrichment analysis: A knowledge-based approach for interpreting genome-wide expression profiles. *Proc. Natl. Acad. Sci. U. S. A.* 102: 15545–15550.
18. Argüello, R. J., A. J. Combes, R. Char, J. P. Gigan, A. I. Baaziz, E. Bousiquot, V. Camosseto, B. Samad, J.

Tsui, P. Yan, S. Boissonneau, D. Figarella-Branger, E. Gatti, E. Tabouret, M. F. Krummel, and P. Pierre. 2020. SCENITH: A Flow Cytometry-Based Method to Functionally Profile Energy Metabolism with Single-Cell Resolution. *Cell Metab.* 32: 1063-1075.e7.

19. Mensurado, S., M. Rei, T. Lanca, M. Ioannou, N. Gonçalves-Sousa, H. Kubo, M. Malissen, V. Papayannopoulos, K. Serre, and B. Silva-Santos. 2018. Tumor-associated neutrophils suppress pro-tumoral IL-17+ γδ T cells 1 through induction of oxidative stress. *PLoS Biol* 16: 1–21.
20. Curtis, C., S. P. Shah, S. F. Chin, G. Turashvili, O. M. Rueda, M. J. Dunning, D. Speed, A. G. Lynch, S. Samarajiwa, Y. Yuan, S. Gräf, G. Ha, G. Haffari, A. Bashashati, R. Russell, S. McKinney, S. Aparicio, J. D. Brenton, I. Ellis, D. Huntsman, S. Pinder, L. Murphy, H. Bardwell, Z. Ding, L. Jones, B. Liu, I. Papatheodorou, S. J. Sammut, G. Wishart, S. Chia, K. Gelmon, C. Speers, P. Watson, R. Blamey, A. Green, D. MacMillan, E. Rakha, C. Gillett, A. Grigoriadis, E. De Rinaldis, A. Tutt, M. Parisien, S. Troup, D. Chan, C. Fielding, A. T. Maia, S. McGuire, M. Osborne, S. M. Sayalero, I. Spiteri, J. Hadfield, L. Bell, K. Chow, N. Gale, M. Kovalik, Y. Ng, L. Prentice, S. Tavaré, F. Markowetz, A. Langerød, E. Provenzano, A. Purushotham, A. L. Børresen-Dale, and C. Caldas. 2012. The genomic and transcriptomic architecture of 2,000 breast tumours reveals novel subgroups. *Nature* 486: 346–352.
21. Newman, A. M., C. B. Steen, C. L. Liu, A. J. Gentles, A. A. Chaudhuri, F. Scherer, M. S. Khodadoust, M. S. Esfahani, B. A. Luca, D. Steiner, M. Diehn, and A. A. Alizadeh. 2019. Determining cell type abundance and expression from bulk tissues with digital cytometry. *Nat. Biotechnol.* 37: 773–782.
22. Wickham, H. 2016. ggplot2 Elegant Graphics for Data Analysis. *Springer* Book.
23. Therneau, T. M., and P. M. Grambsch. 2000. Modeling Survival Data: Extending the Cox Model. *Springer* Book.
24. Sun, L., T. Kees, A. S. Almeida, B. Liu, X. Y. He, D. Ng, X. Han, D. L. Spector, I. A. McNeish, P. Gimotty, S. Adams, and M. Egeblad. 2021. Activating a collaborative innate-adaptive immune response to control metastasis. *Cancer Cell* 39: 1361-1374.e9.
25. Theisen, D. J., S. T. Ferris, C. G. Briseño, N. Kretzer, A. Iwata, K. M. Murphy, and T. L. Murphy. 2019. Batf3-dependent genes control tumor rejection induced by dendritic cells independently of cross-presentation. *Cancer Immunol. Res.* 7: 29–39.
26. Hildner, K., B. T. Edelson, W. E. Purtha, M. Diamond, H. Matsushita, M. Kohyama, B. Calderon, B. U. Schraml, E. R. Unanue, M. S. Diamond, R. D. Schreiber, T. L. Murphy, and K. M. Murphy. 2008. Batf3 Deficiency Reveals a Critical Role for CD8 + Dendritic Cells in Cytotoxic T Cell Immunity. *Science (80-.).* 322: 1097–1100.
27. Sanin, D. E., Y. Ge, E. Marinkovic, A. M. Kabat, A. Castoldi, G. Caputa, K. M. Grzes, J. D. Curtis, E. A. Thompson, S. Willenborg, S. Dichtl, S. Reinhardt, A. Dahl, E. L. Pearce, S. A. Eming, A. Gerbaulet, A. Roers, P. J. Murray, and E. J. Pearce. 2022. A common framework of monocyte-derived macrophage activation. *Sci. Immunol.* 7.
28. Revel, M., C. Sautès-Fridman, W. H. Fridman, and L. T. Roumenina. 2022. C1q+ macrophages: passengers or drivers of cancer progression. *Trends in Cancer* 8: 517–526.
29. Werba, G., D. Weissinger, E. A. Kawaler, E. Zhao, D. Kalfakakou, S. Dhara, L. Wang, H. B. Lim, G. Oh, X. Jing, N. Beri, L. Khanna, T. Gonda, P. Oberstein, C. Hajdu, C. Loomis, A. Heguy, M. H. Sherman, A. W. Lund, T. H. Welling, I. Dolgalev, A. Tsirigos, and D. M. Simeone. 2023. Single-cell RNA sequencing reveals the effects of chemotherapy on human pancreatic adenocarcinoma and its tumor microenvironment. *Nat. Commun.* 14: 1–16.
30. Mulder, K., A. A. Patel, W. T. Kong, C. Piot, E. Halitzki, G. Dunsmore, S. Khalilnezhad, S. E. Irac, A. Dubuisson, M. Chevrier, X. M. Zhang, J. K. C. Tam, T. K. H. Lim, R. M. M. Wong, R. Pai, A. I. S. Khalil, P. K. H. Chow, S. Z. Wu, G. Al-Eryani, D. Roden, A. Swarbrick, J. K. Y. Chan, S. Albani, L. Derosa, L. Zitvogel, A. Sharma, J. Chen, A. Silvin, A. Bertoletti, C. Blériot, C. A. Dutertre, and F. Ginhoux. 2021. Cross-tissue single-cell landscape of human monocytes and macrophages in health and disease. *Immunity* 54: 1883-1900.e5.
31. van Elsas, M. J., J. Middelburg, C. Labrie, J. Roelands, G. Schaap, M. Sluijter, R. Tonea, V. Ovcinnikovs, K. Lloyd, J. Schuurman, S. J. Riesenfeld, T. F. Gajewski, N. F. C. C. de Miranda, T. van Hall, and S. H. van der Burg. 2024. Immunotherapy-activated T cells recruit and skewlate-stage activated M1-like macrophagesthat are critical for therapeutic efficacy. *Cancer Cell* 1–19.
32. Kwak, T., F. Wang, H. Deng, T. Condamine, V. Kumar, M. Perego, A. Kossenkov, L. J. Montaner, X. Xu, W. Xu, C. Zheng, L. M. Schuchter, R. K. Amaravadi, T. C. Mitchell, G. C. Karakousis, C. Mulligan, B. Nam, G. Masters, N. Hockstein, J. Bennett, Y. Nefedova, and D. I. Gabrilovich. 2020. Distinct Populations of Immune-Suppressive Macrophages Differentiate from Monocytic Myeloid-Derived Suppressor Cells in Cancer. *Cell Rep.* 33: 108571.
33. Chakraborty, B., J. Byemerwa, J. Shepherd, C. N. Haines, R. Baldi, W. Gong, W. Liu, D. Mukherjee, S. Artham, F. Lim, Y. Bae, O. Brueckner, K. Tavares, S. E. Wardell, B. A. Hanks, C. M. Perou, C. Y. Chang,

and D. P. McDonnell. 2021. Inhibition of estrogen signaling in myeloid cells increases tumor immunity in melanoma. *J. Clin. Invest.* 131.

34. Martinez, F. O., S. Gordon, M. Locati, and A. Mantovani. 2006. Transcriptional Profiling of the Human Monocyte-to-Macrophage Differentiation and Polarization: New Molecules and Patterns of Gene Expression. *J. Immunol.* 177: 7303–7311.
35. Marcovecchio, P. M., G. Thomas, and S. Salek-Ardakani. 2021. CXCL9-expressing tumor-associated macrophages: New players in the fight against cancer. *J. Immunother. Cancer* 9: 1–7.
36. Bae, S., P. S. U. Park, Y. Lee, S. H. Mun, E. Giannopoulou, T. Fujii, K. P. Lee, S. N. Violante, J. R. Cross, and K. H. Park-Min. 2021. MYC-mediated early glycolysis negatively regulates proinflammatory responses by controlling IRF4 in inflammatory macrophages. *Cell Rep.* 35: 109264.
37. Rei, M., N. Gonçalves-Sousa, T. Lança, R. G. Thompson, S. Mensurado, F. R. Balkwill, H. Kulbe, D. J. Pennington, and B. Silva-Santos. 2014. Murine CD27(-) Vγ6(+) γδ T cells producing IL-17A promote ovarian cancer growth via mobilization of protumor small peritoneal macrophages. *Proc. Natl. Acad. Sci. U. S. A.* 27: 3562–3570.
38. Chalupsky, K., and H. Cai. 2005. Endothelial dihydrofolate reductase: Critical for nitric oxide bioavailability and role in angiotensin II uncoupling of endothelial nitric oxide synthase. *Proc. Natl. Acad. Sci. U. S. A.* 102: 9056–9061.
39. Nathan, C., and M. U. Shiloh. 2000. No TitleReactive oxygen and nitrogen intermediates in the relationship between mammalian hosts and microbial pathogens. *Proc. Natl. Acad. Sci. U. S.* 97: 8841–8848.
40. Guiducci, C., A. P. Vicari, S. Sangaletti, G. Trinchieri, and M. P. Colombo. 2005. Redirecting in vivo elicited tumor infiltrating macrophages and dendritic cells towards tumor rejection. *Cancer Res.* 65: 3437–3446.
41. Reis-Sobreiro, M., A. Teixeira da Mota, C. Jardim, and K. Serre. 2021. Bringing Macrophages to the Frontline against Cancer: Current Immunotherapies Targeting Macrophages. *Cells* 10: 2364.
42. Bell, C. R., and S. Zelenay. 2022. COX-2 upregulation by tumour cells post-chemotherapy fuels the immune evasive dark side of cancer inflammation. *Cell Stress* 6: 76–78.
43. Cheng, S., Z. Li, R. Gao, B. Xing, Y. Gao, Y. Yang, S. Qin, L. Zhang, H. Ouyang, P. Du, L. Jiang, B. Zhang, Y. Yang, X. Wang, X. Ren, J. X. Bei, X. Hu, Z. Bu, J. Ji, and Z. Zhang. 2021. A pan-cancer single-cell transcriptional atlas of tumor infiltrating myeloid cells. *Cell* 184: 792-809.e23.
44. Yang, S., M. Wang, Y. Hua, J. Li, H. Zheng, M. Cui, N. Huang, Q. Liu, and Q. Liao. 2024. Advanced insights on tumor-associated macrophages revealed by single-cell RNA sequencing: The intratumor heterogeneity, functional phenotypes, and cellular interactions. *Cancer Lett.* 584: 216610.
45. Nasir, I., C. McGuinness, A. R. Poh, M. Ernst, P. K. Darcy, and K. L. Britt. 2023. Tumor macrophage functional heterogeneity can inform the development of novel cancer therapies. *Trends Immunol.* 44: 971–985.
46. Sadik, A., L. F. Somarribas Patterson, S. Öztürk, S. R. Mohapatra, V. Panitz, P. F. Secker, P. Pfänder, S. Loth, H. Salem, M. T. Prentzell, B. Berdel, M. Iskar, E. Faessler, F. Reuter, I. Kirst, V. Kalter, K. I. Foerster, E. Jäger, C. R. Guevara, M. Sobeh, T. Hielscher, G. Poschet, A. Reinhardt, J. C. Hassel, M. Zapatka, U. Hahn, A. von Deimling, C. Hopf, R. Schlichting, B. I. Escher, J. Burhenne, W. E. Haefeli, N. Ishaque, A. Böhme, S. Schäuble, K. Thedieck, S. Trump, M. Seiffert, and C. A. Opitz. 2020. IL4I1 Is a Metabolic Immune Checkpoint that Activates the AHR and Promotes Tumor Progression. *Cell* 182: 1252-1270.e34.
47. Bill, R., P. Wirapati, M. Messemaker, W. Roh, B. Zitti, F. Duval, M. Kiss, J. C. Park, T. M. Saal, J. Hoelzl, D. Tarussio, F. Benedetti, S. Tissot, L. Kandalaft, M. Varrone, G. Ciriello, T. A. McKee, Y. Monnier, M. Mermod, E. M. Blaum, I. Gushterova, A. L. K. Gonye, N. Hacohen, G. Getz, T. R. Mempel, A. M. Klein, R. Weissleder, W. C. Faquin, P. M. Sadow, D. Lin, S. I. Pai, M. Sade-Feldman, and M. J. Pittet. 2023. CXCL9:SPP1 macrophage polarity identifies a network of cellular programs that control human cancers. *Science (80-.).* 381: 515–524.
48. Klug, F., H. Prakash, P. E. Huber, T. Seibel, N. Bender, N. Halama, C. Pfirschke, R. H. Voss, C. Timke, L. Umansky, K. Klapproth, K. Schäkel, N. Garbi, D. Jäger, J. Weitz, H. Schmitz-Winnenthal, G. J. Hämmerling, and P. Beckhove. 2013. Low-Dose Irradiation Programs Macrophage Differentiation to an iNOS+/M1 Phenotype that Orchestrates Effective T Cell Immunotherapy. *Cancer Cell* 24: 589–602.
49. Palmieri, E. M., M. Gonzalez-cotto, W. A. Baseler, L. C. Davies, B. Ghesquière, N. Maio, C. M. Rice, T. A. Rouault, T. Cassel, R. M. Higashi, A. N. Lane, T. W. Fan, D. A. Wink, and D. W. Mcvicar. 2020. Nitric oxide orchestrates metabolic rewiring in M1 macrophages by targeting aconitase 2 and pyruvate dehydrogenase. *Nat. Commun.* .
50. Kotsafti, A., M. Scarpa, I. Castagliuolo, and M. Scarpa. 2020. Reactive oxygen species and antitumor immunity—from surveillance to evasion. *Cancers (Basel).* 12: 1–16.
51. Kratochvill, F., G. Neale, J. M. Haverkamp, L. A. Van de Velde, A. M. Smith, D. Kawauchi, J. McEvoy, M. F. Roussel, M. A. Dyer, J. E. Qualls, and P. J. Murray. 2015. TNF Counterbalances the Emergence of M2 Tumor Macrophages. *Cell Rep.* 12: 1902–1914.

52. Johansson, A., J. Hamzah, C. J. Payne, and R. Ganss. 2012. Tumor-targeted TNFα stabilizes tumor vessels and enhances active immunotherapy. *Proc. Natl. Acad. Sci. U. S. A.* 109: 7841–7846.
53. Moore, R. J., D. M. Owens, G. Stamp, C. Arnott, F. Burke, N. East, H. Holdsworth, L. Turner, B. Rollins, M. Pasparakis, G. Kollias, and F. Balkwill. 1999. Mice deficient in tumor necrosis factor-α are resistant to skin carcinogenesis. *Nat. Med.* 5: 828–831.
54. Bergers, G., and L. E. Benjamin. 2003. Tumorigenesis and the angiogenic switch. *Nat. Rev. Cancer* 3: 401–410.
55. Sharma, N., X. Fan, O. T. Atolagbe, Z. Ge, K. N. Dao, P. Sharma, and J. P. Allison. 2024. ICOS costimulation in combination with CTLA-4 blockade remodels tumor-associated macrophages toward an antitumor phenotype. *J. Exp. Med.* 221.
56. Cassetta, L., and T. Kitamura. 2018. Targeting tumor-associated macrophages as a potential strategy to enhance the response to immune checkpoint inhibitors. *Front. Cell Dev. Biol.* 6: 1–6.
57. Salvagno, C., M. Ciampricotti, S. Tuit, C. S. Hau, A. van Weverwijk, S. B. Coffelt, K. Kersten, K. Vrijland, K. Kos, T. Ulas, J. Y. Song, C. H. Ooi, D. Rüttinger, P. A. Cassier, J. Jonkers, J. L. Schultze, C. H. Ries, and K. E. de Visser. 2019. Therapeutic targeting of macrophages enhances chemotherapy efficacy by unleashing type I interferon response. *Nat. Cell Biol.* 21: 511–521.
58. Sánchez-Paulete, A. R., J. Mateus-Tique, G. Mollaoglu, S. R. Nielsen, A. Marks, A. Lakshmi, J. A. Khan, C. M. Wilk, L. Pia, A. Baccarini, M. Merad, and B. D. Brown. 2022. Targeting Macrophages with CAR T Cells Delays Solid Tumor Progression and Enhances Antitumor Immunity. *Cancer Immunol. Res.* 10: 1354–1369.
59. Sharma, A., J. J. W. Seow, C. A. Dutertre, R. Pai, C. Blériot, A. Mishra, R. M. M. Wong, G. S. N. Singh, S. Sudhagar, S. Khalilnezhad, S. Erdal, H. M. Teo, A. Khalilnezhad, S. Chakarov, T. K. H. Lim, A. C. Y. Fui, A. K. W. Chieh, C. P. Chung, G. K. Bonney, B. K. P. Goh, J. K. Y. Chan, P. K. H. Chow, F. Ginhoux, and R. DasGupta. 2020. Onco-fetal Reprogramming of Endothelial Cells Drives Immunosuppressive Macrophages in Hepatocellular Carcinoma. *Cell* 183: 377-394.e21.
60. Blériot, C., S. Chakarov, and F. Ginhoux. 2020. Determinants of Resident Tissue Macrophage Identity and Function. *Immunity* 52: 957–970.
61. Franklin, R. a, W. Liao, A. Sarkar, M. V Kim, M. R. Bivona, K. Liu, E. G. Pamer, and M. O. Li. 2014. The cellular and molecular origin of tumor-associated macrophages. *Science* 344: 921–5.
62. Zhu, Y., J. M. Herndon, D. K. Sojka, K. W. Kim, B. L. Knolhoff, C. Zuo, D. R. Cullinan, J. Luo, A. R. Bearden, K. J. Lavine, W. M. Yokoyama, W. G. Hawkins, R. C. Fields, G. J. Randolph, and D. G. DeNardo. 2017. Tissue-Resident Macrophages in Pancreatic Ductal Adenocarcinoma Originate from Embryonic Hematopoiesis and Promote Tumor Progression. *Immunity* 47: 323-338.e6.
63. Kim, N., H. K. Kim, K. Lee, Y. Hong, J. H. Cho, J. W. Choi, J. Il Lee, Y. L. Suh, B. M. Ku, H. H. Eum, S. Choi, Y. La Choi, J. G. Joung, W. Y. Park, H. A. Jung, J. M. Sun, S. H. Lee, J. S. Ahn, K. Park, M. J. Ahn, and H. O. Lee. 2020. Single-cell RNA sequencing demonstrates the molecular and cellular reprogramming of metastatic lung adenocarcinoma. *Nat. Commun.* 11.
64. Chen, Y. P., J. H. Yin, W. F. Li, H. J. Li, D. P. Chen, C. J. Zhang, J. W. Lv, Y. Q. Wang, X. M. Li, J. Y. Li, P. P. Zhang, Y. Q. Li, Q. M. He, X. J. Yang, Y. Lei, L. L. Tang, G. Q. Zhou, Y. P. Mao, C. Wei, K. X. Xiong, H. B. Zhang, S. Da Zhu, Y. Hou, Y. Sun, M. Dean, I. Amit, K. Wu, D. M. Kuang, G. B. Li, N. Liu, and J. Ma. 2020. Single-cell transcriptomics reveals regulators underlying immune cell diversity and immune subtypes associated with prognosis in nasopharyngeal carcinoma. *Cell Res.* 30: 1024–1042.
65. Laviron, M., M. Petit, E. Weber-Delacroix, A. J. Combes, A. R. Arkal, S. Barthélémy, T. Courau, D. A. Hume, C. Combadière, M. F. Krummel, and A. Boissonnas. 2022. Tumor-associated macrophage heterogeneity is driven by tissue territories in breast cancer. *Cell Rep.* 39.

Figure Legends

Fig. 1. Phenotype and function of BMDM activated with MCT.

(A) Scheme of *in vitro* polarization of bone marrow-derived macrophages (BMDM) to M0, M1, M2, and MCT phenotypes. **(B)** Proportion of polarized BMDM expressing TNF-α, iNOS, ICAM-1, MHC-II, PD-L1, and PD-L2. Note that TNF-α, was assessed 6h post-polarization while all others were assessed 24h post-polarization. **(C)** BMDM and E0771 tumor cells co-cultured for 48h, then analyzed by flow cytometry to identify live E0771 tumor cells. **(D)** Viability, assessed by cell tracker blue, and **(E)** cell death, assessed by 7-AAD staining, of E0771 tumor cells incubated with supernatants of the four BMDM phenotypes for 72h. **(F)** Quantification of glucose, lactate, ATP, and pH from the supernatants of the four BMDM phenotypes. **(G)** Metabolic dependencies or capacities of the four BMDM phenotypes analyzed by SCENITH™. **(H)** Viability of the four BMDM phenotypes assessed by flow cytometry using a live-dead dye. Data are representative of two to ten independent experiments. Individual values from independent experiments and median are plotted. Non-parametric two-tailed Mann-Whitney test were performed, and *$p < 0.05$, **$p < 0.01$, ***$p < 0.001$, ****$p < 0.0001$ are shown.

Fig. 2. Sustained MCT treatment induces tumor regression in a macrophage-dependent manner.

(A) Scheme of *in vivo* experiment setup with the MCT schedule. **(B)** Individual tumor growth curves after E0771 cell transplantation in WT animals, with or without treatment with TLR3 ligand (Poly I:C) and anti-CD40 agonist, alone or in combination. The right graph represents the ratio of tumor size at the time of treatment (T0) and three days later (T3/T0) for each individual mouse. **(C)** Numbers of responders (orange) *versus* non-responders (black) as a function of the size of the tumor at the time of treatment. The numbers in the bars represent the total number of mice in each group. **(D)** Individual tumor growth curves from NT (black), or animals treated once (1x, yellow), twice (2x, orange), or three times (3x, red) every three days. **(E)** Ratio of tumor size at the time of MCT (T0) and three days (T3/T0), six days (T6/T0), or nine days (T9/T0) later, as a function of the number of MCT injections, for each individual mouse. **(F)** Kaplan-Meier survival graph for E0771-bearing mice receiving one, two, or three MCT injections. **(G)** Scheme of *in vivo* experiment setup with the treatment and macrophage depletion using clodronate-liposome injection schedule. **(H)** One representative experiment of individual tumor growth curves after E0771 cell transplantation and MCT (orange) or MCT with clodronate-liposome (blue) injections. The bottom graph represents the tumor size ratio (T3/T0) and includes animals receiving MCT with control PBS-liposomes (red). Data compile two to three independent experiments, except data in panel (B), which was done only once. Individual values from individual mouse and median are plotted. Non-parametric two-tailed Mann-Whitney test were performed, and *p < 0.05, **p < 0.01, ***p < 0.001, ****p <0.0001 are shown.

Fig. 3. ScRNA-seq analysis with myeloid cell annotation and distribution across conditions.

Full description of the samples used for scRNA-seq analysis are described in supplementary figure 4. **(A)** tSNE visualization of the selected myeloid cell subsets (clusters *Lyz2* #0Mac, *Cd209a* #1cDC2, *Nos2* #3Mac, *Ccl22* #4cDC1, *Clec9a* #6cDC1, *Siglech* #7 plasmacytoid, and *Cpa3* #8 mast cells identified in Fig. S3A-B). tSNE plots represent total (across all groups) and myeloid cells selected from each individual group: tumors without treatment (NT), tumors collected after 12 or 72 hours post-treatment (MCT-12h and MCT-72h, respectively), and progressive tumors without treatment (PT). Cells are colored by a shared nearest neighbor (SNN) modularity optimization-based clustering algorithm. **(B)** Proportion of the main myeloid clusters identified across samples from the four conditions (NT, MCT-12h, MCT-72h, and PT). **(C)** Individual tumor growth curves after E0771 cell transplantation in *Batf3* KO animals, with or without MCT. The right graph represents the ratio of tumor size at the time of treatment (T0) and three days later (T3/T0) for each individual *Batf3* KO mice. Data in panel (C) compile two independent experiments. Individual values from individual mouse and median are plotted. Non-parametric two-tailed Mann-Whitney test was performed, and ***p < 0.001 is shown.

Fig. 4. Macrophage characterization and transient anti-tumor features.

(A) tSNE visualization of the selected tumor-infiltrating macrophage and monocyte subsets (clusters *Lyz2* #0Mac and *Nos2* #3Mac identified in Fig. S3A-B). tSNE plots represent total (across all groups) and macrophages selected from each individual group (NT, MCT-12h, MCT-72h, and PT). **(B)** Proportion of the main tumor-infiltrating macrophage and monocyte clusters identified across samples from the four conditions (NT, MCT-12h, MCT-72h, and PT). **(C)** Dot plot representing scaled average gene expression (blue color intensity) and percentage of cells (dot size) expressing featured markers across clusters represented in 4A. **(D)** Heatmap representing a pseudobulk analysis of tumor-infiltrating macrophage and monocyte subset clusters as shown in 4A. Colors indicate the scaled gene set scores for each hallmark pathway. **(E)** Dot plot representing scaled average gene signature scores (color) and percentage of cells (dot size) with a positive score across clusters represented in 4A. The violin plots and the gene signatures are depicted in the table in Fig. S4F.

Fig. 5. Kinetics of in vivo antitumor determinants induced by MCT in TAMs.

(A) Scheme of *in vivo* experiment setup with the MCT schedules. **(C)** Proportion of iNOS, CD38, TNF-α, or MHC-II positive cells within TAMs + TAMonos assessed by flow cytometry as depicted in Fig. S5A. Tumor-infiltrated macrophages and monocytes were isolated from WT animals left NT, or after one MCT injections at day 1, 3, and 4 (D4 x1), or two MCT injections at day 4 (D4 x2). WT mice received E0771 cell transplantation followed by MCT in the presence of iNOS inhibitors **(D)**, the antioxidant N-acetyl cysteine (NAC) **(E)**, or blocking anti-TNF-α antibody **(F)**, as described in Fig. S5B. The plots on the right side shows the ratio of tumor size at the time of treatment and three (T3/T0), six (T6/T0), and nine (T9/T0) days later for each individual mouse. The left side shows the Kaplan-Meier survival graph for E0771-bearing mice receiving MCT in the presence of each inhibitor type: iNOS inhibitors **(D)**, NAC **(E)**, and blocking anti-TNF-α antibody **(F)**. Data in B-E compile at least two independent experiments for each condition. Individual values from individual mouse and median are plotted. Non-parametric two-tailed Mann-Whitney test were performed, and $*p < 0.05$, $**p < 0.01$, $***p < 0.001$, $****p < 0.0001$ are shown.

Fig. 6. Self-antigen presentation by tumor cells and T cell activation *in vivo*.

(A) Representative dot plots showing the concentration of IFN-α (left) and IFN-β (right) in the supernatant of BMDM polarized in various conditions. **(B)** Representative flow cytometry plots of H-2Kb molecules (left plots) and H-2Kb-SIINFEKL complexes (right plots) on OVA-E0771 cells and GFP-E0771 control cells incubated overnight with supernatants of M0-, M1-, M2-, or MCT-BMDMs. **(C)** Expression of H-2Kb-SIINFEKL complexes in OVA-E0771 cells induced by M0, M1, M2, and MCT supernatants in the presence of blocking anti-IFN-α receptor, anti-IFN-γ, or anti-TNF-α antibodies. **(D)** Expression of *Cxcl9* mRNA measured by qPCR in FACS-sorted CD45+CD11b+CD3e-CD19-NK1.1-Ly6G- cells from tumor samples collected from NT, or 1, 3, 4, and 7 days post-MCT animals. **(E)** Ratio of tumor size three days post-MCT (T3/T0) for each individual *Rag2* KO x *γc* KO mice (left plot) and *TCRα* KO mice (right plot). **(F)** Frequency of tumor-infiltrating IFN-γ+ CD8 T cells from NT animals and from three and seven days post-MCT animals. **(G)** WT mice received E0771 cell transplantation followed by MCT in the presence of depleting anti-CD8 antibodies as depicted in Fig. S6E. **(H)** Kaplan-Meier survival graph for E0771-bearing mice treated with MCT and rechallenged 50 days later on the contralateral mammary fat pad with a new inoculation of E0771 cells. Individual values from individual mouse and median are plotted. Non-parametric two-tailed Mann-Whitney test were performed, and $*p < 0.05$, $**p < 0.01$, $***p < 0.001$ are shown.

Figure 1

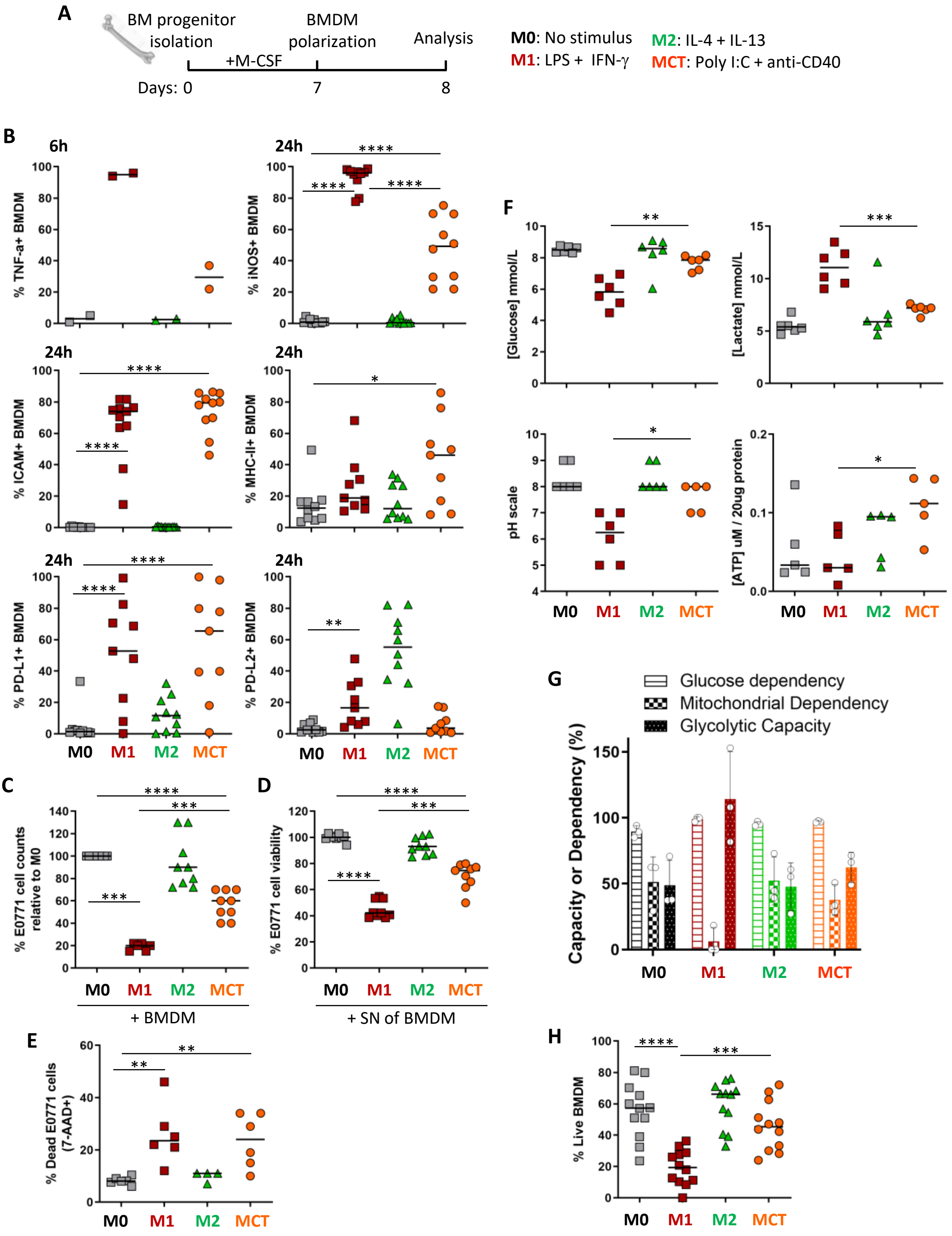
A
BM progenitor isolation
+M-CSF
BMDM polarization
Analysis
Days: 0
7
8
M0: No stimulus
M1: LPS + IFN-γ
M2: IL-4 + IL-13
MCT: Poly I:C + anti-CD40
B
6h
% TNF-a+ BMDM
24h
% iNOS+ BMDM
% ICAM+ BMDM
% MHC-II+ BMDM
% PD-L1+ BMDM
% PD-L2+ BMDM
0
20
40
60
80
100
****
***
**
*
M0
M1
M2
MCT
C
% E0771 cell counts relative to M0
0
20
40
60
80
100
120
140
+ BMDM
D
% E0771 cell viability
+ SN of BMDM
E
% Dead E0771 cells (7-AAD+)
F
[Glucose] mmol/L
[Lactate] mmol/L
pH scale
[ATP] uM / 20ug protein
0.0
0.1
0.2
G
Glucose dependency
Mitochondrial Dependency
Glycolytic Capacity
Capacity or Dependency (%)
0
50
100
150
H
% Live BMDM

Figure 2

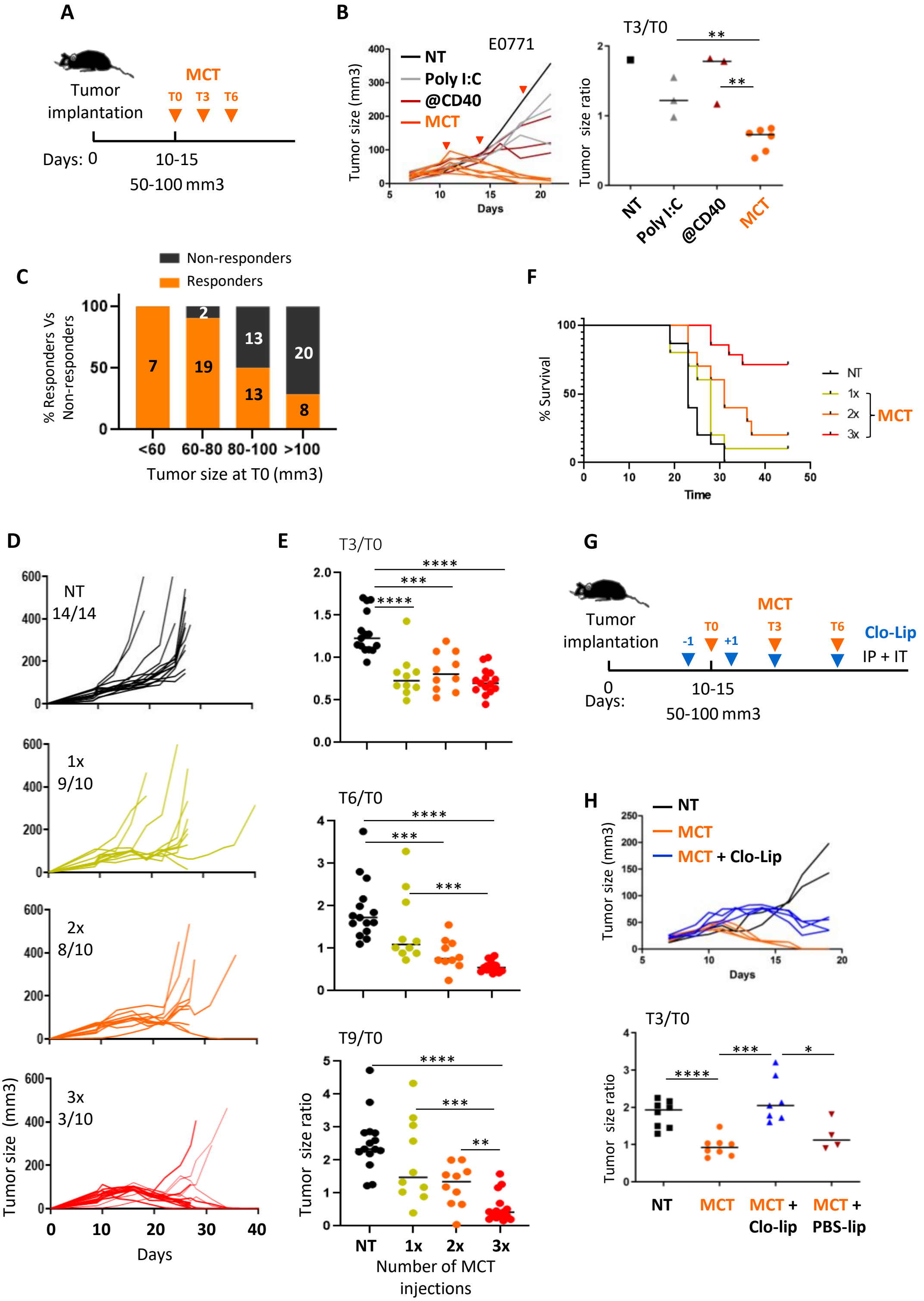
A
Tumor implantation
MCT
T0
T3
T6
Days: 0
10-15
50-100 mm3
B
E0771
NT
Poly I:C
@CD40
MCT
Tumor size (mm3)
400
300
200
100
0
5
10
15
20
Days
T3/T0
**
**
Tumor size ratio
2
1
0
NT
Poly I:C
@CD40
MCT
C
Non-responders
Responders
% Responders Vs Non-responders
100
50
0
7
2
19
13
13
20
8
<60
60-80
80-100
>100
Tumor size at T0 (mm3)
F
% Survival
100
50
0
0
10
20
30
40
50
Time
NT
1x
2x
3x
MCT
D
600
400
200
0
NT
14/14
1x
9/10
2x
8/10
3x
3/10
Tumor size (mm3)
0
10
20
30
40
Days
E
T3/T0
2.0
1.5
1.0
0.5
0.0
****
***
****
T6/T0
4
3
2
1
0
****
***
***
T9/T0
5
4
3
2
1
0
****
***
**
Tumor size ratio
NT
1x
2x
3x
Number of MCT injections
G
Tumor implantation
MCT
T0
T3
T6
-1
+1
Clo-Lip
IP + IT
0
Days:
10-15
50-100 mm3
H
NT
MCT
MCT + Clo-Lip
Tumor size (mm3)
250
200
150
100
50
0
5
10
15
20
Days
T3/T0
4
3
2
1
0
****
***
*
Tumor size ratio
NT
MCT
MCT + Clo-lip
MCT + PBS-lip

Figure 3

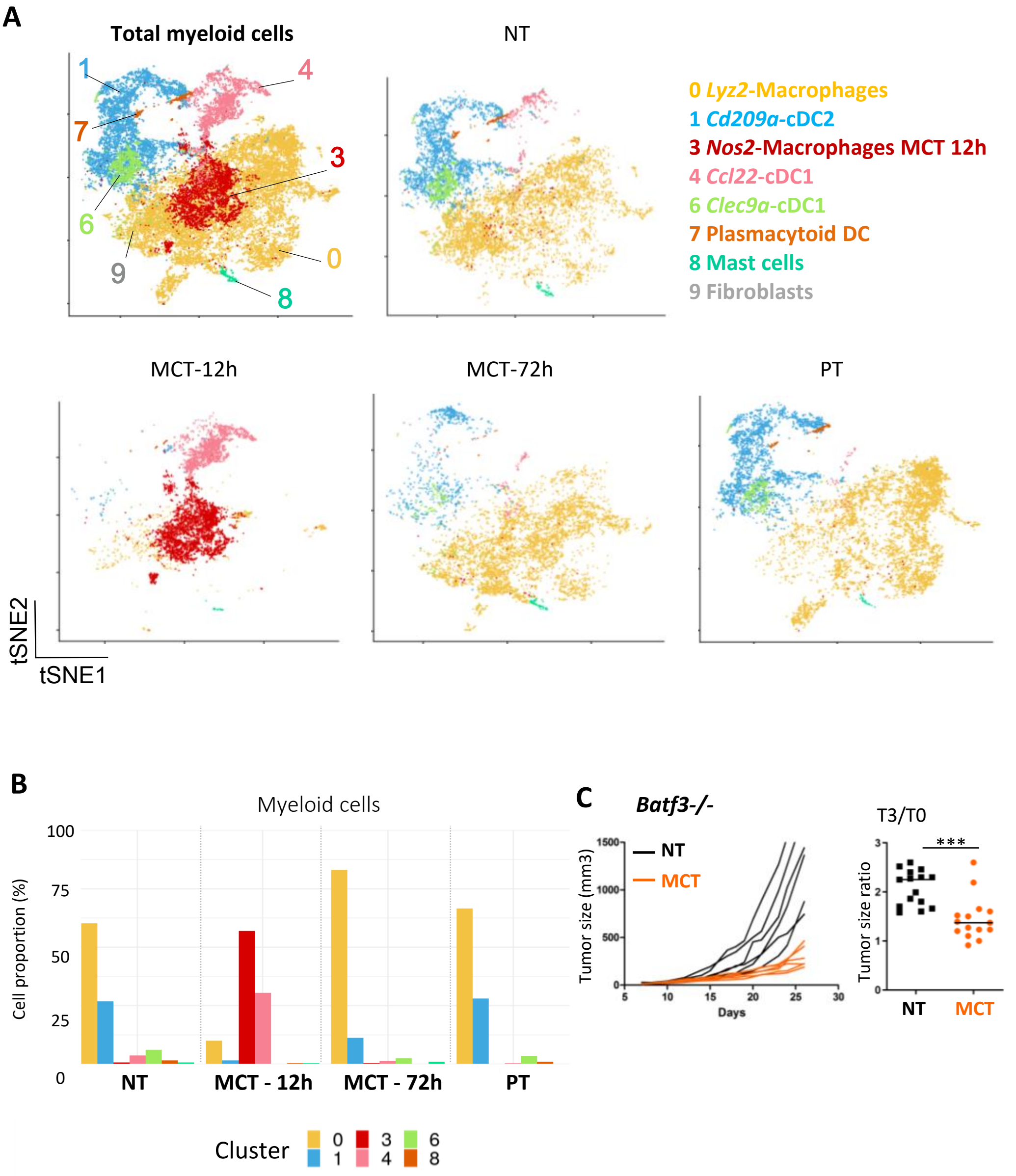
A
Total myeloid cells
NT
MCT-12h
MCT-72h
PT
1
4
7
3
6
9
0
8
0 *Lyz2*-Macrophages
1 *Cd209a*-cDC2
3 *Nos2*-Macrophages MCT 12h
4 *Ccl22*-cDC1
6 *Clec9a*-cDC1
7 Plasmacytoid DC
8 Mast cells
9 Fibroblasts
tSNE2
tSNE1
B
Myeloid cells
Cell proportion (%)
100
75
50
25
0
NT
MCT - 12h
MCT - 72h
PT
Cluster
0
1
3
4
6
8
C
Batf3-/-
NT
MCT
Tumor size (mm3)
1500
1000
500
0
5
10
15
20
25
30
Days
T3/T0
Tumor size ratio
3
2
1
0
***
NT
MCT

Figure 4

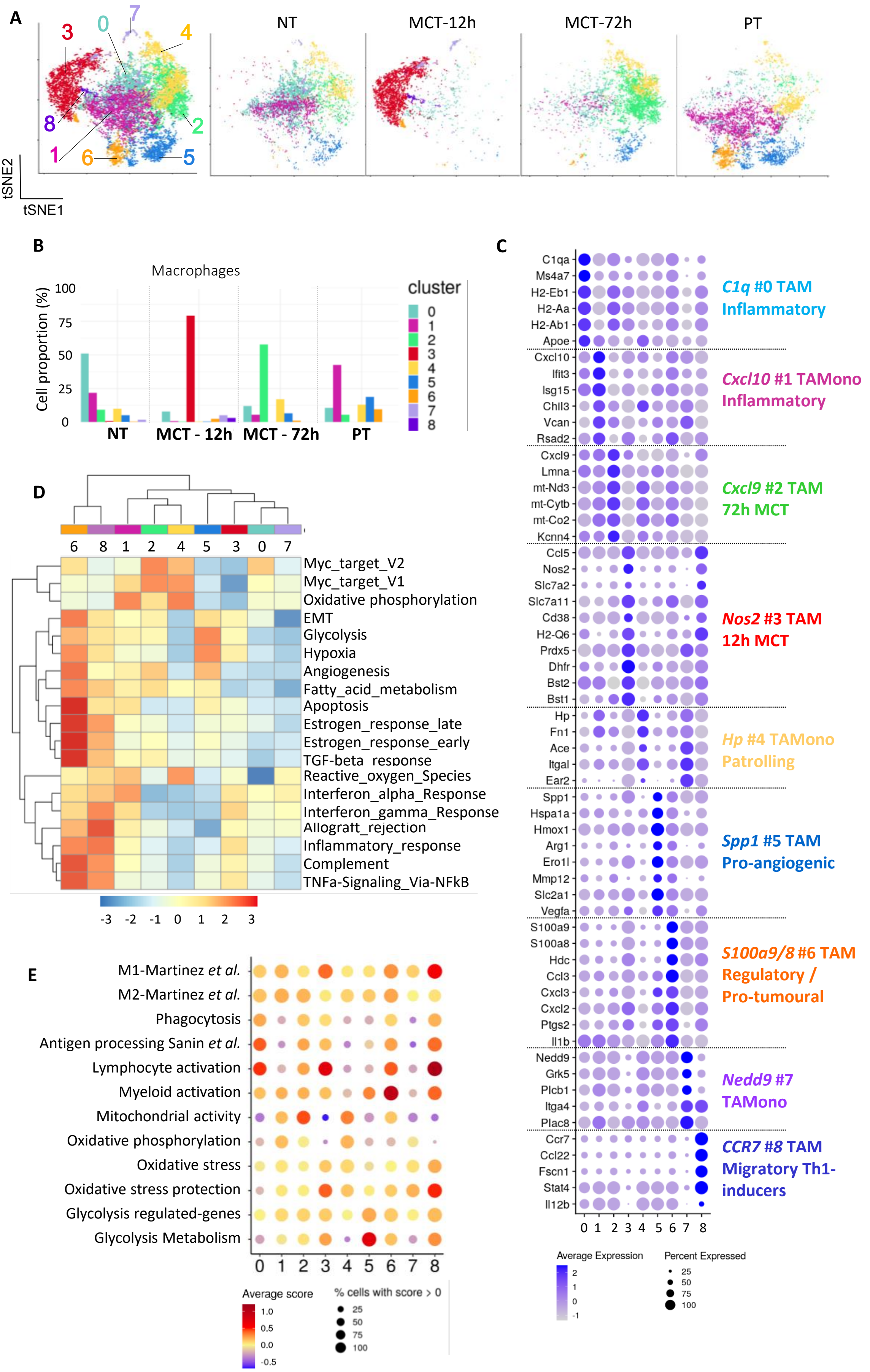
A
3
0
7
4
8
2
1
6
5
tSNE2
tSNE1
NT
MCT-12h
MCT-72h
PT
B
Macrophages
Cell proportion (%)
100
75
50
25
0
NT
MCT - 12h
MCT - 72h
PT
cluster
0
1
2
3
4
5
6
7
8
C
C1qa
Ms4a7
H2-Eb1
H2-Aa
H2-Ab1
Apoe
Cxcl10
Ifit3
Isg15
Chil3
Vcan
Rsad2
Cxcl9
Lmna
mt-Nd3
mt-Cytb
mt-Co2
Kcnn4
Ccl5
Nos2
Slc7a2
Slc7a11
Cd38
H2-Q6
Prdx5
Dhfr
Bst2
Bst1
Hp
Fn1
Ace
Itgal
Ear2
Spp1
Hspa1a
Hmox1
Arg1
Ero1l
Mmp12
Slc2a1
Vegfa
S100a9
S100a8
Hdc
Ccl3
Cxcl3
Cxcl2
Ptgs2
Il1b
Nedd9
Grk5
Plcb1
Itga4
Plac8
Ccr7
Ccl22
Fscn1
Stat4
Il12b
0 1 2 3 4 5 6 7 8
C1q #0 TAM Inflammatory
Cxcl10 #1 TAMono Inflammatory
Cxcl9 #2 TAM 72h MCT
Nos2 #3 TAM 12h MCT
Hp #4 TAMono Patrolling
Spp1 #5 TAM Pro-angiogenic
S100a9/8 #6 TAM Regulatory / Pro-tumoural
Nedd9 #7 TAMono
CCR7 #8 TAM Migratory Th1-inducers
Average Expression
2
1
0
-1
Percent Expressed
25
50
75
100
D
6 8 1 2 4 5 3 0 7
Myc_target_V2
Myc_target_V1
Oxidative phosphorylation
EMT
Glycolysis
Hypoxia
Angiogenesis
Fatty_acid_metabolism
Apoptosis
Estrogen_response_late
Estrogen_response_early
TGF-beta_response
Reactive_oxygen_Species
Interferon_alpha_Response
Interferon_gamma_Response
Allograft_rejection
Inflammatory_response
Complement
TNFa-Signaling_Via-NFkB
-3 -2 -1 0 1 2 3
E
M1-Martinez et al.
M2-Martinez et al.
Phagocytosis
Antigen processing Sanin et al.
Lymphocyte activation
Myeloid activation
Mitochondrial activity
Oxidative phosphorylation
Oxidative stress
Oxidative stress protection
Glycolysis regulated-genes
Glycolysis Metabolism
0 1 2 3 4 5 6 7 8
Average score
1.0
0.5
0.0
-0.5
% cells with score > 0
25
50
75
100

Figure 5

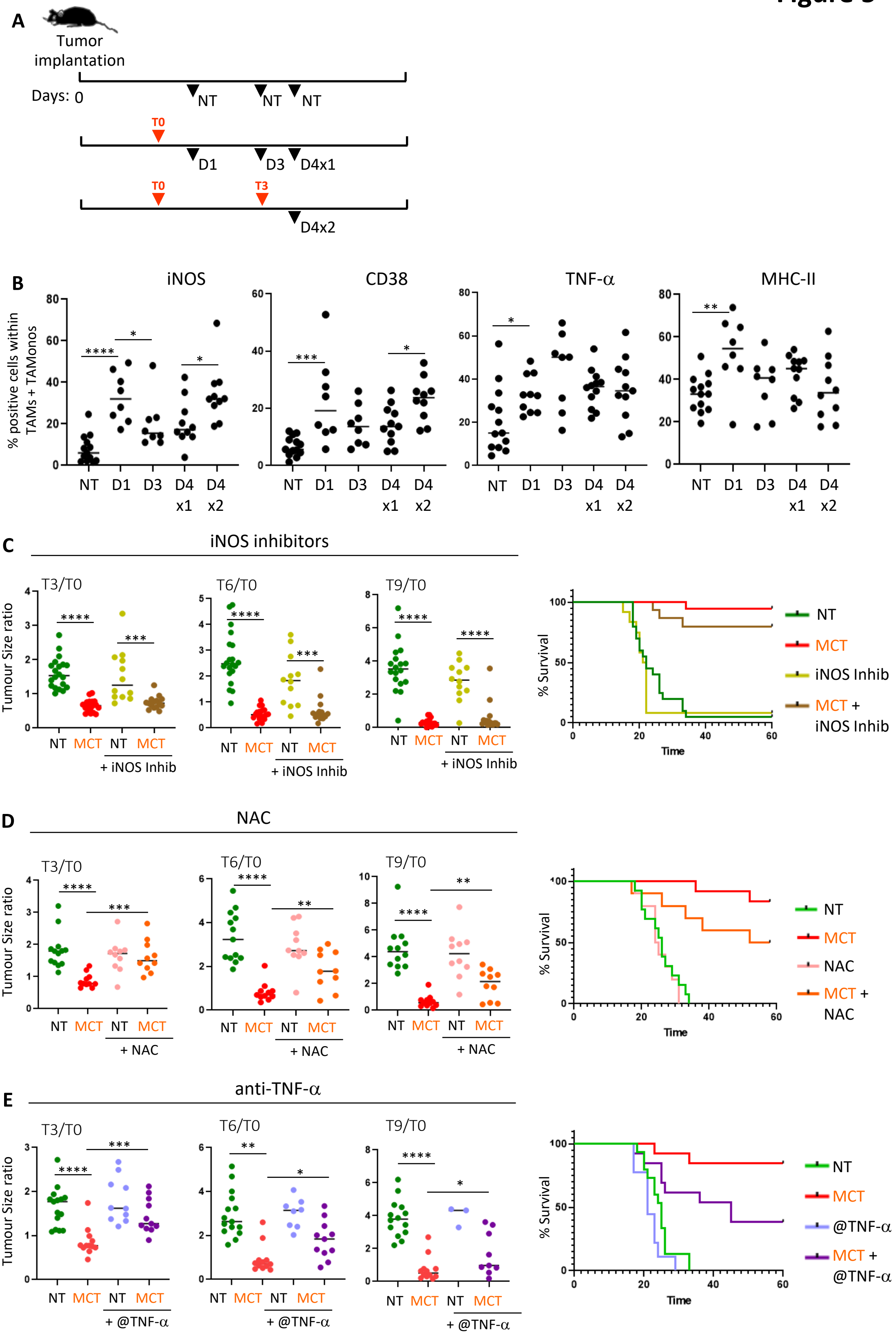

A
Tumor implantation
Days: 0
NT
NT
NT
T0
D1
D3
D4x1
T0
T3
D4x2
B
iNOS
CD38
TNF-α
MHC-II
% positive cells within TAMs + TAMonos
NT
D1
D3
D4 x1
D4 x2
C
iNOS inhibitors
T3/T0
T6/T0
T9/T0
Tumour Size ratio
NT
MCT
+ iNOS Inhib
% Survival
Time
NT
MCT
iNOS Inhib
MCT + iNOS Inhib
D
NAC
T3/T0
T6/T0
T9/T0
Tumour Size ratio
NT
MCT
+ NAC
% Survival
Time
NT
MCT
NAC
MCT + NAC
E
anti-TNF-α
T3/T0
T6/T0
T9/T0
Tumour Size ratio
NT
MCT
+ @TNF-α
% Survival
Time
NT
MCT
@TNF-α
MCT + @TNF-α

Figure 6

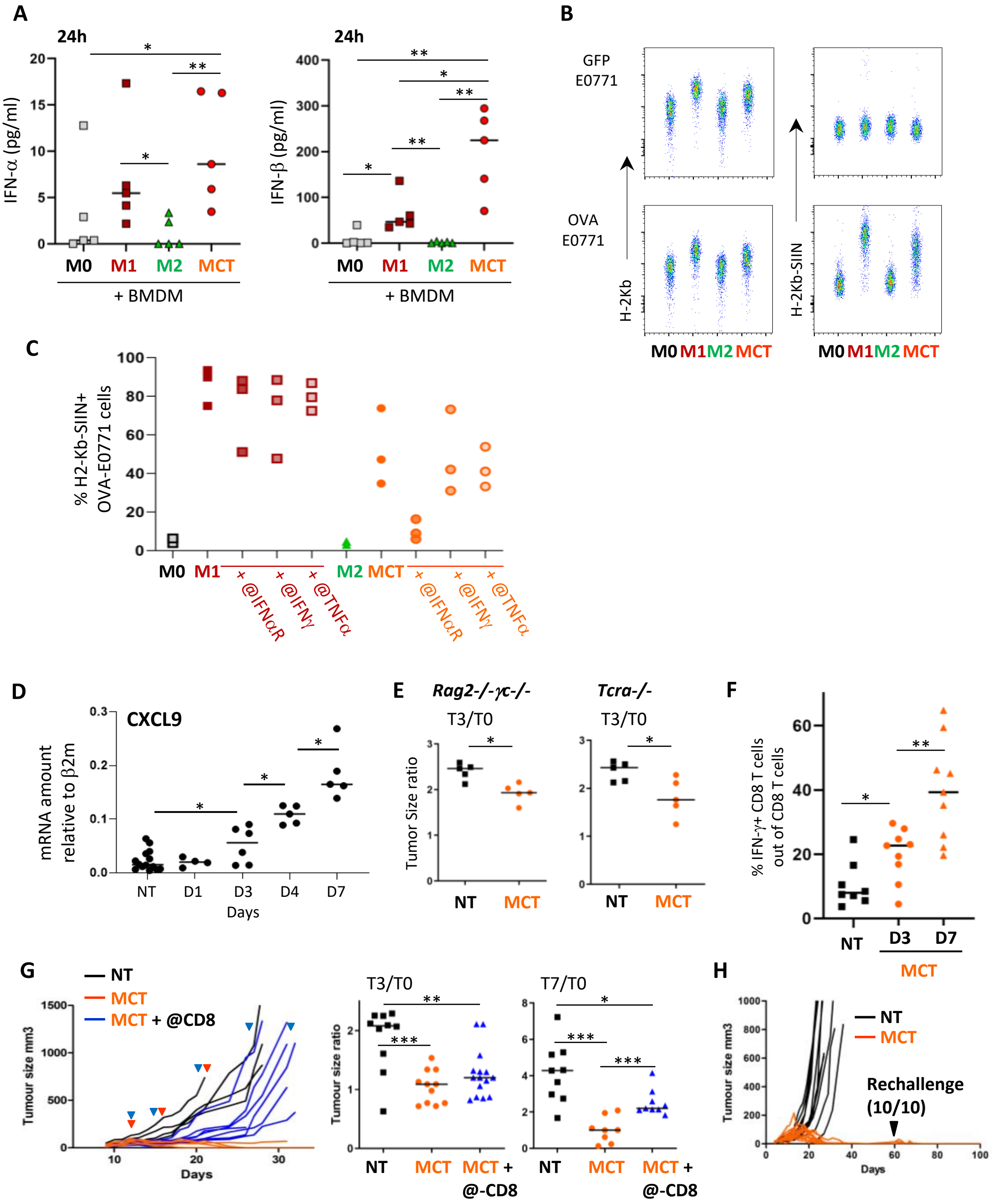
A
24h
IFN-α (pg/ml)
20
15
10
5
0
*
**
*
M0
M1
M2
MCT
+ BMDM
24h
IFN-β (pg/ml)
400
300
200
100
0
**
*
**
**
*
M0
M1
M2
MCT
+ BMDM
B
GFP
E0771
OVA
E0771
H-2Kb
H-2Kb-SIIN
M0 M1 M2 MCT
M0 M1 M2 MCT
C
% H2-Kb-SIIN+
OVA-E0771 cells
100
80
60
40
20
0
M0
M1
+ @IFNαR
+ @IFNγ
+ @TNFα
M2
MCT
+ @IFNαR
+ @IFNγ
+ @TNFα
D
CXCL9
mRNA amount
relative to β2m
0.3
0.2
0.1
0.0
*
*
*
NT
D1
D3
D4
D7
Days
E
Rag2-/-γc-/-
T3/T0
Tumor Size ratio
3
2
1
0
*
NT
MCT
Tcra-/-
T3/T0
3
2
1
0
*
NT
MCT
F
% IFN-γ+ CD8 T cells
out of CD8 T cells
60
40
20
0
*
**
NT
D3
D7
MCT
G
NT
MCT
MCT + @CD8
Tumour size mm3
1500
1000
500
0
10
20
30
Days
T3/T0
Tumour size ratio
2
1
0
**
***
NT
MCT
MCT +
@-CD8
T7/T0
8
6
4
2
0
*
***
***
NT
MCT
MCT +
@-CD8
H
Tumour size mm3
1000
800
600
400
200
0
0
20
40
60
80
100
Days
NT
MCT
Rechallenge
(10/10)

Supplementary Materials for:

Sustained macrophage reprogramming is required for CD8 T cell-dependent long-term tumor eradication

Carolina Jardim, Marta Bica, *et al.*

Corresponding authors: Karine Serre karine.serre@gimm.pt,
Nuno L. Barbosa-Morais nuno.morais@gimm.pt

This file includes:

Figs. S1 to S9

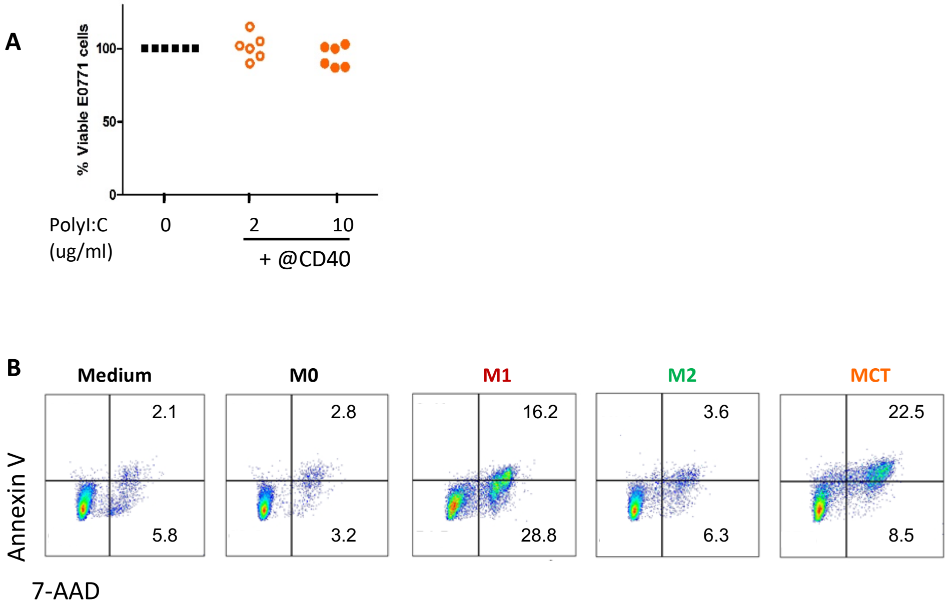

Supplementary Figure 1: Assessment of E0771 Sensitivity to TLR3 and CD40 agonists.

Supplementary Fig. 1. Assessment of E0771 sensitivity to TLR3 and CD40 agonists.

(A) Viability of E0771 tumor cells assessed by CellTracker Blue after incubation with TLR3 ligand (Poly I:C) at concentrations of 2 µg/ml and 10 µg/ml, and agonist anti-CD40 antibody at 2.5 µg/ml for 48 hours. Data are from two independent experiments. **(B)** Representative flow cytometry plots showing cell death of E0771 tumor cells, assessed by annexin V and 7-AAD staining, following incubation with supernatants from the four BMDM phenotypes (M0, M1, M2, and MCT) for 72 hours. MCT-polarized BMDM supernatant actively induced tumor cell killing *in vitro*.

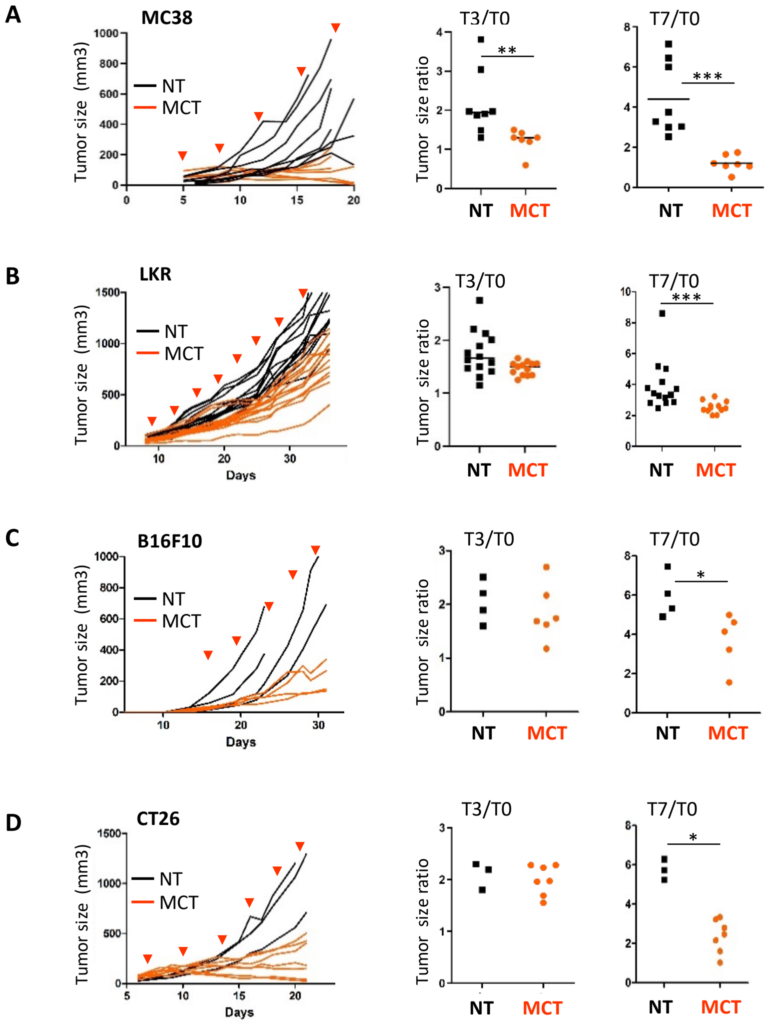

Supplementary Figure 2: Sustained MCT induces tumor growth control in various types of cancers from different genetic backgrounds.

Supplementary Fig. 2. Sustained MCT induces tumor growth control in various types of cancers from different genetic backgrounds

Mice were injected with tumor cells and treated with MCT when tumors reached 50–100 mm^2. Individual tumor growth curves with or without MCT are shown for **(A)** MC38 (colorectal cancer cell line from C57BL6/J background), **(B)** LKR (lung cancer cell line from 123xC57BL6/J background), **(C)** B16F10 (melanoma cancer cell line from C57BL6/J background), **(D)** CT26 (colorectal cancer cell line from BALB/c background). The dot plots on the right represents the ratio of tumor size at the time of treatment (T0) and either three (T3/T0) or seven (T7/T0) days later, for each individual mouse.

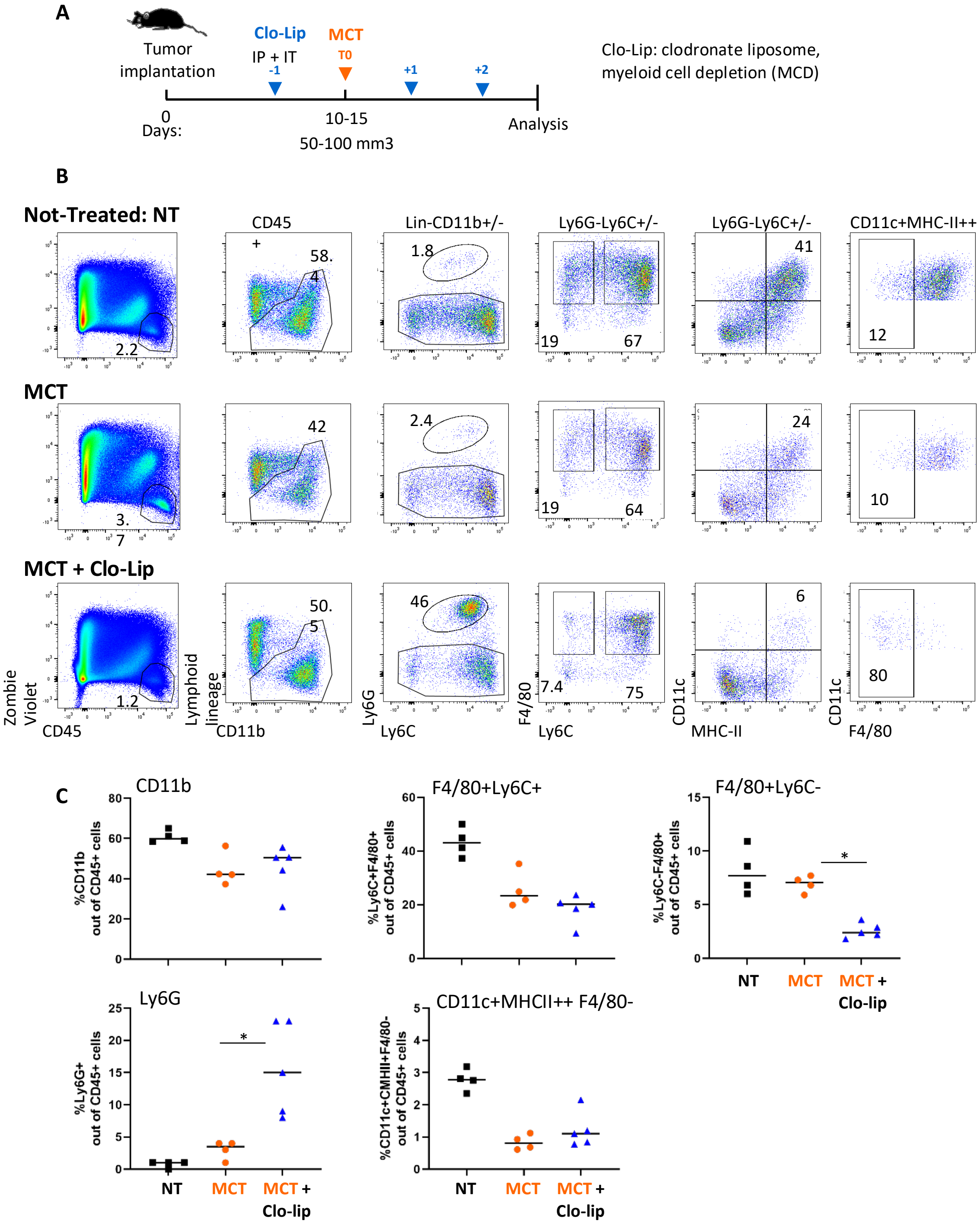

Supplementary Figure 3: Characterization of the effect of myeloid cell depletion in E0771 tumors *in vivo*.

Supplementary Figure 3 – Characterization of the effect of myeloid cell depletion in E0771 tumors in vivo. **(A)** Scheme of in vivo experiment setup with the treatment and macrophage depletion using clodronate-liposome injection schedule. **(B)** Representative flow cytometry gating strategy to identify total myeloid cells (lymphoid lineage- CD11b+), neutrophils (Ly6G+), mono-macrophages (F4/80+Ly6C+), macrophages (F4/80+Ly6C-) and

DC (CD11c+MHCII++ F4/80-). **(C)** The dot plots represent the proportion of various myeloid cell subsets out of CD45+ cells for each individual mouse, with 4 to 5 animals per group.

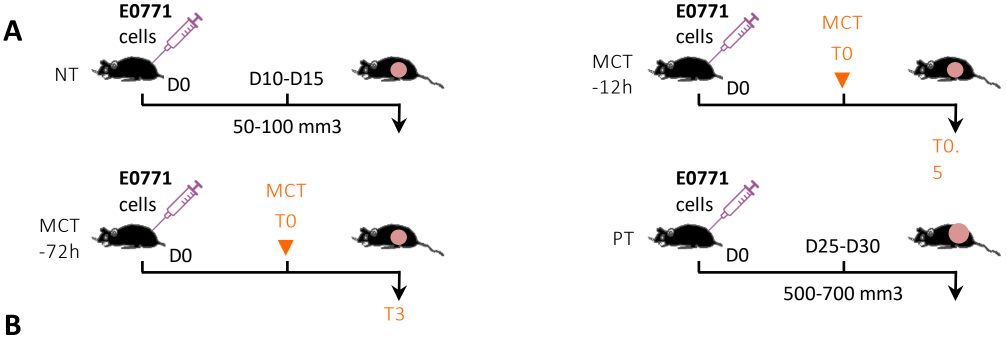

B

	Sample	Tumor size	% Live cells	T3/T0 ratio	Mouse ID	Sorting date	#cells	Mean Reads	Median UMI	Median Genes	Total genes	Sequencing saturation (%)
1	NT	129	77%	2,04	3590 n1	12/04/2019	1923	91096	10838	2542	16711	74.7
2	MCT-72h	61,9	87%	1,04	3590 n2	12/04/2019	1897	89716	12111	2856	16380	70.7
3	PT	594	60%	-	3634 n1	15/07/2019	8500	63736	10430	2671	18964	65.9
4	NT	129,3	68%	1,61	3866 n2	15/07/2019	6756	57770	9882	2569	18797	64.1
5	MCT-72h	67,3	67%	0,95	3867 n5	15/07/2019	6191	62118	8925	2625	18652	68.2
6	PT	656	92%	-	4084 n1	25/09/2019	1635	64580	10560	2591	16181	64.1
7	PT	590	92%	-	4084 n2	25/09/2019	2120	69446	10986	2656	16358	67.0
8	NT	141,31	88%	1,87	4168 n1	25/09/2019	4373	63633	10203	2566	17809	69.2
9	MCT-72h	78,41	87%	1,05	4170 n1	25/09/2019	2880	67617	11338	2809	16878	68.4
10	NT	94.64	91%	-	7181 n3	24/03/2023	3855	123273	16765	3798	21676	75.2
11	MCT-12h	93.3	93%	-	7181 n1	24/03/2023	4476	90072	14978	3470	21977	70.1
12	MCT-12h	87	93%	-	7182 n4	24/03/2023	4328	100639	16979	3721	22235	71.2

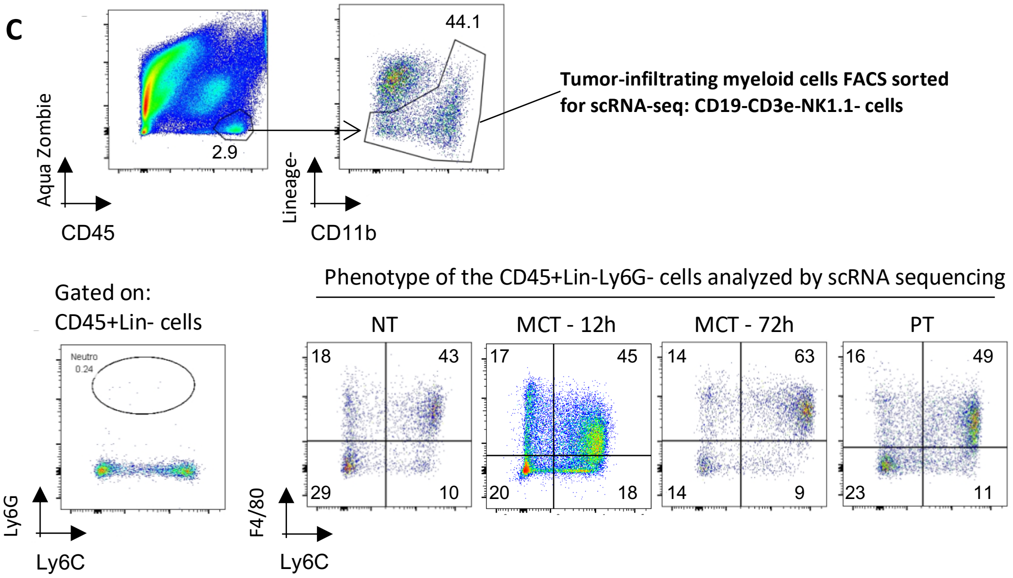

Tumor-infiltrating myeloid cells FACS sorted for scRNA-seq: CD19-CD3e-NK1.1- cells

Supplementary Figure 4: Gating Strategy to sort myeloid subsets for scRNA-seq and metadata of each samples.

Supplementary Fig. 4. Gating Strategy to sort myeloid subsets for scRNA-seq and metadata of each sample. **(A)** Scheme of the *in vivo* experiment setup for each individual group: tumors without treatment (NT), tumors collected 12 or 72 hours post-treatment (MCT-12h and MCT-72h, respectively), and progressive tumors without treatment (PT). **(B)** Table representative of each sample, indicating the tumor size at the time of collection, percentage of live cells, the ratio of tumor size three days post-MCT (T3/T0), mouse ID, sorting date, number of cells sequenced per group, mean reads, median of unique molecular identifiers (UMI), median genes, total genes, and the percentage of sequencing saturation. **(C)** A permissive gating approach was used to sort all live tumor-infiltrating myeloid cells (CD45+CD19-CD3-NK1.1- cells) for scRNA-seq.

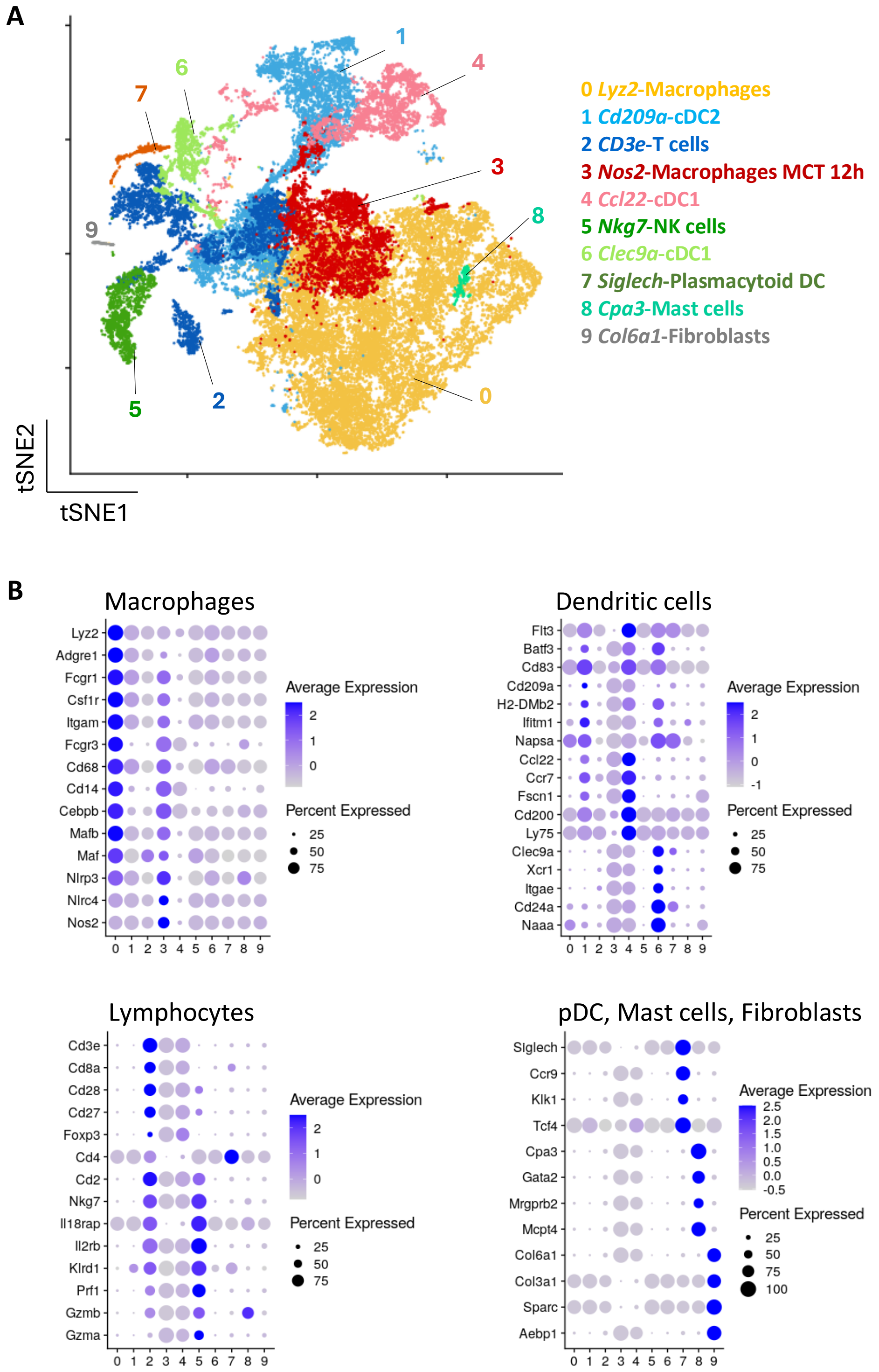

Supplementary Figure 5: ScRNAseq cell annotations.

Supplementary Fig. 5. ScRNA-seq cell annotations.

(A) tSNE visualization of the total 40,446 cells spanning all four conditions for which quality-controlled mRNA profiles were obtained. Nine tumor-associated immune cell subsets were identified based on bona fide marker genes and clustered as follows: Lyz2 #0 macrophages, Cd209a #1 cDC2, CD3e #2 T cells, Nos2 #3 macrophages, Ccl22 #4 cDC1, Nkg7 #5 NK cells, Clec9a #6 cDC1, Siglech #7 plasmacytoid DC, Cpa3 #8 mast cells, and Col6a1 #9 fibroblasts. **(B)** Dot plots representing scaled average lineage-specific gene expression (blue color intensity) and the percentage of cells (dot size) expressing featured markers across clusters represented in S3A. Representative lineage-specific genes are shown in four dot plots identifying macrophages, dendritic cells, lymphocytes, plasmacytoid DC (pDC), mast cells, and fibroblasts.

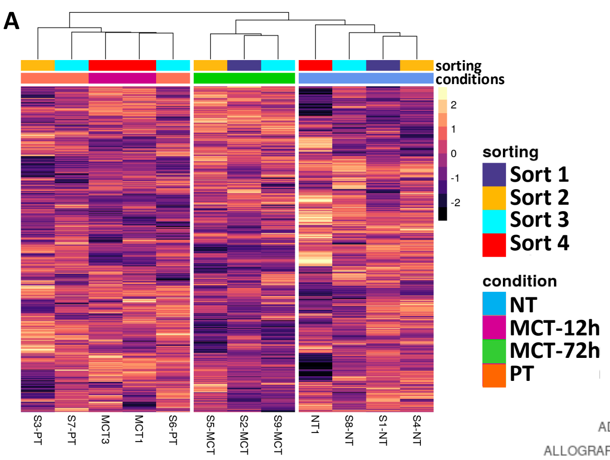

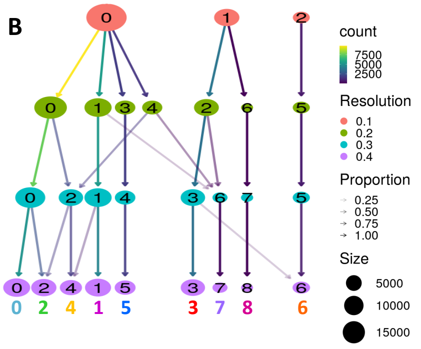

C

	NT	MCT-12h	MCT-72h	PT	Total	%
0	3550	357	649	697	5253	22.4
1	1524	26	296	2802	4648	19.8
2	650	22	3137	365	4174	17.8
3	42	3559	1	7	3609	15.4
4	691	14	925	860	2490	10.6
5	348	24	351	1233	1956	8.3
6	29	112	57	630	828	3.5
7	117	235	0	2	354	1.5
8	2	139	0	0	141	0.6
Total	6953	4488	5416	6596	23453	

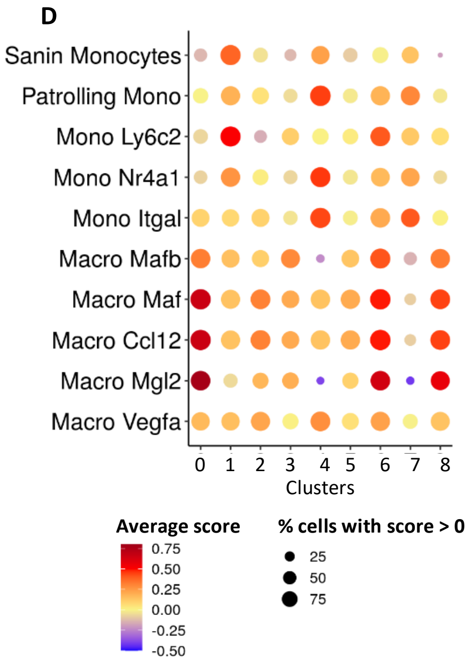

Supplementary Figure 6: Macrophage characterization and Transient anti-tumor features.

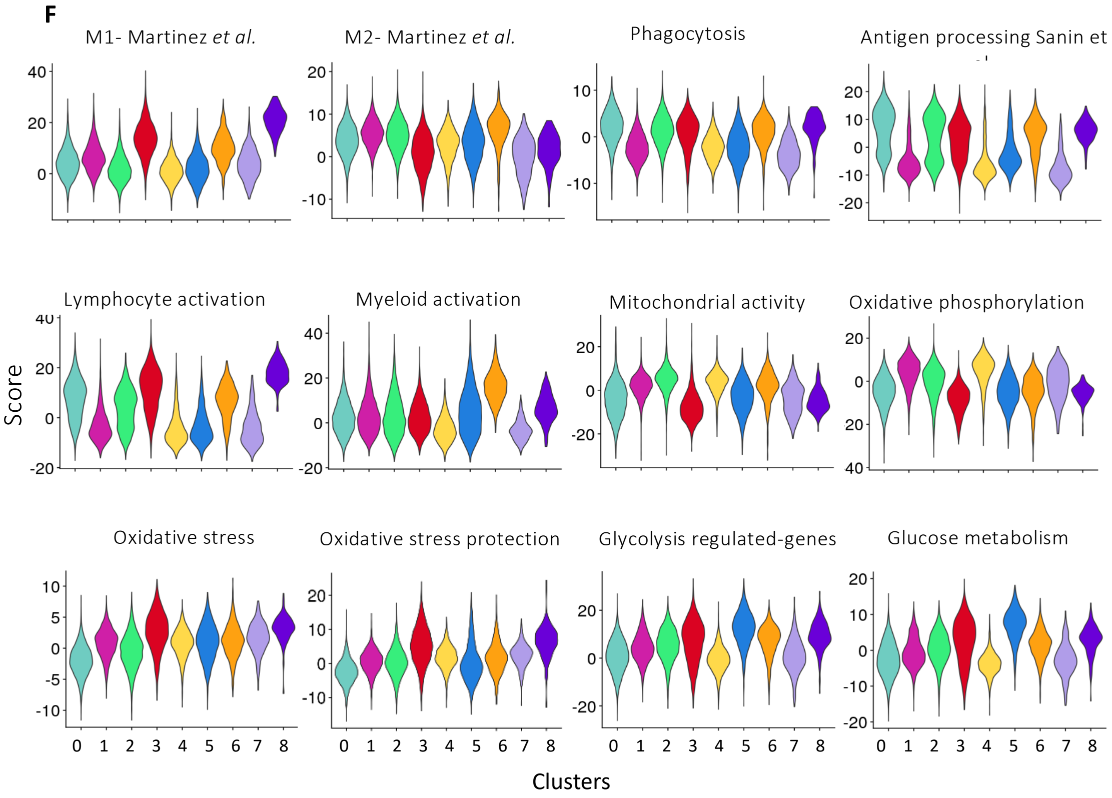

Signature Name	Gene List
M1-Martinez *et al*	Ccr7, Il2ra, Il15ra, Il7r, Cxcl10, Cxcl9, Ccl19, Tnf, Ccl5, Il12b, Il6, Igf1, Fas, Birc3, Gadd45g, Slc7a5, Slc2a6, Slc31a2, Pla1a, Hsd11b1, Ak3, Sphk1, Pfkfb3, Psme2, Pfkp, Psmb9, Psma2, Oas2, Ptx3, Igfbp4, Pdgfa, Edn1, Inhba, Hesx1, Irf1, Atf3, Irf7
M2-Martinez *et al*	Tgfbr2, Hrh1, Tlr5, Msr1, Cxcr4, P2ry14, Mrc1, Igf1, Slc4a7, Slc38a6, Ctsc, Hexb, Lipa, Adk, Hnmt, Tpst2, Cerk, Lta4h, Alox15, Hs3st1, Tgfbi, Chn2, Fn1, Fgl2, Gas7, Egr2, Maf
Phagocytosis	Gsn, Itgam, Cd74, Tlr2, Axl, Itgb2, Slamf7, C1qa, Cyba, Sirpa
Antigen processing Sanin *et al*	H2-K1, B2m, Klrd1, Lgmn, Ctsb, H2-Aa, H2-Ab1, H2-Eb1, H2-DMa, H2-DMb1, H2-DMb2, H2-Oa, H2-Ob, Cd74, Ctsl, Ciita
Lymphocyte activation	Cd80, Cd86, Icosl, Cd40, Ccl5, H2-Aa, H2-Eb1, H2-Ab1, Cd74, B2m, Il12b, Cxcl9, Cxcl10, Cxcl16, H2-Q6, H2-Q7
Myeloid activation	Csf1, Pf4, Il1b, Il6, Cxcl1, Cxcl2, Cxcl3, Ccl2, Ccl3, Ccl4, Ccl6, Ccl9, Ccl12, Nlrp3, Ptgs2, Trem2, Mrc1
Mitochondrial activity	mt-Nd3, mt-Nd1, mt-Nd2, mt-Cytb, mt-Nd4, mt-Nd5, mt-Co2, mt-Nd4l, mt-Co1, mt-Co3, mt-Atp6
Oxidative Phosphorylation	Atp5a1, Atp5c1, Atp5e, Atp5g2, Atp5h, Atp1a1, Atp1a3, Atp6v1b2, Atp5f1, Atp11b, Cox6c, Cox7a2, Cox7b, Cox17, mt-Cytb, Ndufa4, Ndufa6, Ndufa12, Ndufa13, Ndufb2, Ndufb5, Ndufb10, Ndufb11, Ndufs2, Uqcr11, Uqcrh
Oxidative Stress	Nox1, Cybb, Nox4, Mpo, Nos1, Nos2, Nos3
Oxidative Stress Protection	Gpx1, Gsr, Gstm1, Gsto1, Prdx1, Prdx5, Prdx6, Sod2, Srxn1, Txn1, Txnrd1, Slc7a2, Slc7a11, Dhfr
Glycolysis regulated-genes	Adora2b, Ak3, Ak4, Aldh7a1, Aldoa, Arpp19, Aurka, Igfbp7, Capn5, Cenpa, Chpf2, Chst2, Dld, Depdc1a, Eno1, Eno2, Fam162a, Gale, Galk2, Galk2, Gfpt1, Gpc1, Hax1, Hdlbp, Hk2, Hmmr, Idua, Kdelr3, Kif20a, Ldha, Mif, Nasp, Ndufv3, Nt5e, P4ha1, P4ha2, Pdk3, Pfkp, Pgam1, Pgk1, Pkp2, Plod2, Pmm2, Polr3k, Prps1, Pygl, Qsox1, Rars, Rbck1, Rpe, Rragd, Sap30, Slc37a4, Slc5a3, Stc2, Tpi1, Txn1, Ugp2
Glycolysis Metabolism	Aldoa, Eno1, Gapdh, Hk1, Hk2, Ldha, Pgk1, Pkm, Slc2a1, Tpi1

Supplementary Figure 6: Macrophage characterization and Transient anti-tumor features.

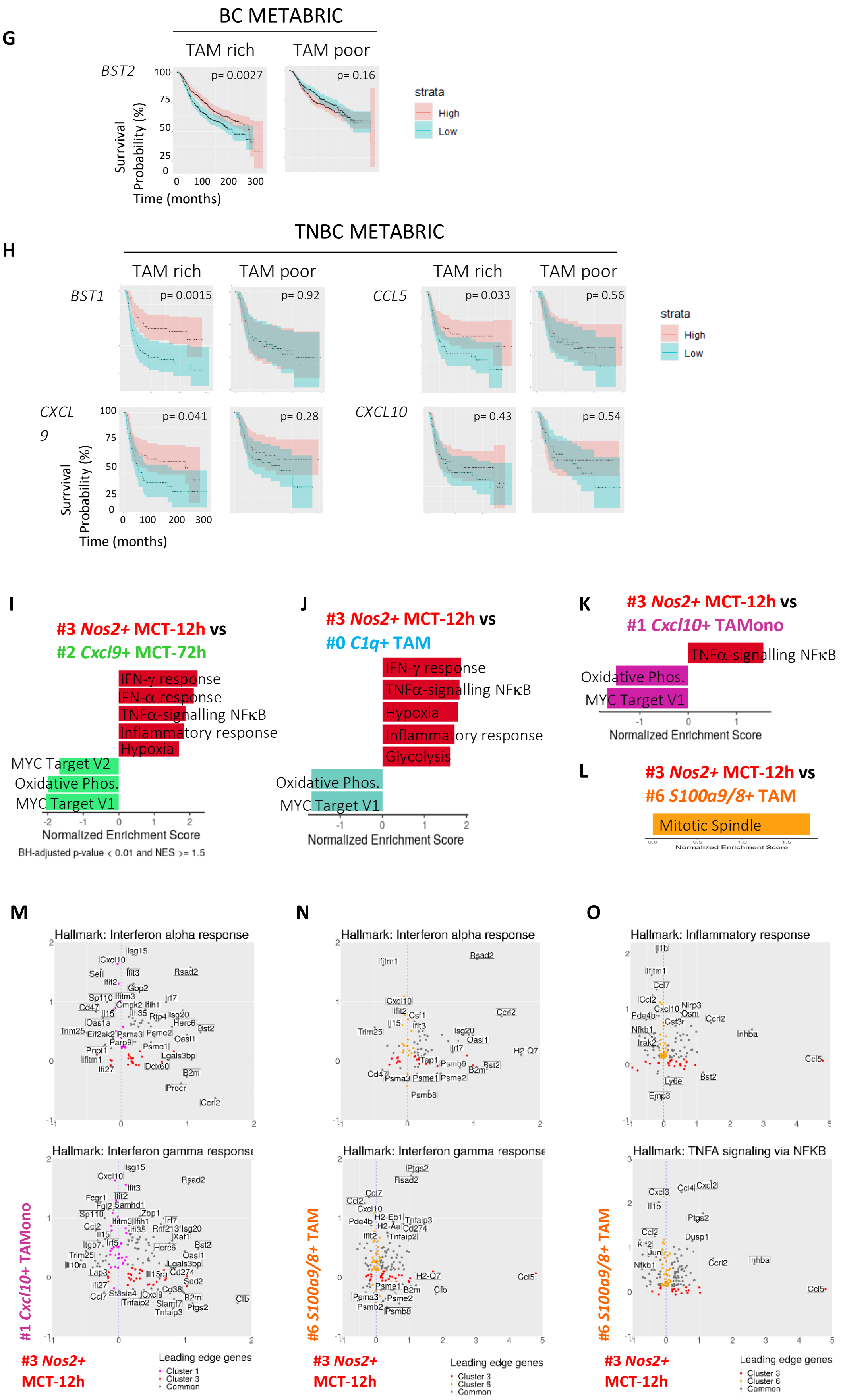

Supplementary Figure 6: Macrophage characterization and transient anti-tumor features.

Supplementary Fig. 6. Macrophage characterization and transient anti-tumor features.

(A) Heatmap representing a pseudobulk analysis of scRNA-seq data of the selected tumor-infiltrating macrophage and monocyte subsets (clusters Lyz2 #0Mac and Nos2 #3Mac identified in Fig. S3A-B), analyzing a total of 23,453 cells (6953 from NT, 4488 from MCT-12h, 5416 from MCT-72h and 6596 from PT). The heatmap emphasizes the clustering of samples from different conditions based on the expression of the top 3000 most variable genes (HVGs). **(B)** Cluster tree depicting the unsupervised clustering analysis for the macrophage subset at the single-cell level, using the top 25 principal components. We chose a resolution of 0.4, which grouped cells across conditions into 9 distinct clusters. Each cluster corresponds to a node in the tree, with edges connecting nodes to indicate cell transitions between clusters at different resolutions. Nodes are colored by clustering resolution; edge opacity and color reflect the proportion and number of cells, respectively, transitioning to the child cluster; node size corresponds to the number of cells within the cluster. **(C)** Table representing the number of cells for each cluster within each group (NT, MCT-12h, MCT-72h, PT). **(D)** Dot plot representing scaled average specific gene signature scores (color intensity) and the percentage of cells (dot size) with a positive score across clusters represented in S4B. Monocytes were separated from macrophages using previously published signatures (9)(17). **(E)** Dot plot representing results from nine gene set enrichment analyses (GSEA), with each analysis resulting from the comparison of each cluster against the others. Color represents upregulated (red) or downregulated (blue) pathways, and size represents -log10 of the Benjamini-Hochberg corrected p-value plus a small constant (10^-9). **(F)** Violin plots of specific gene signatures, as detailed in the table below, for the nine tumor-infiltrating macrophage and monocyte clusters. **(G)** Overall survival curves of METABRIC breast cancer patients, with primary tumors estimated by CIBERSORTx to be relatively rich (left panel – TAM rich) and poor (right panel – TAM poor) in tumor-associated macrophages (TAMs), stratified by their expression of gene *BST2* (v. Materials & Methods). **(H)** Overall survival curves of METABRIC triple-negative breast cancer (TNBC) patients only, with primary tumors estimated by CIBERSORTx to be relatively rich (left panels – TAM rich) and poor (right panels – TAM poor) in tumor-associated macrophages (TAMs), stratified by their expression of genes *BST1*, *CCL5*, *CXCL9*, and *CLCX10* (v. Materials & Methods). **(I-J-K-L)** Bar plots representing GSEA comparing #3 Nos2+ MCT-12h versus #2 Cxcl9+ MCT-72h **(I)**, #3 Nos2+ MCT-12h versus #0 C1q+ TAM **(J)**, #3 Nos2+ MCT-12h versus #1 Cxcl10+ TAMono **(K)**, and #3 Nos2+ MCT-12h versus #6 S100a9/8+ TAM **(L)**. Note that for bar plots I, J and K, only hallmark pathways with a Benjamini-Hochberg corrected p-value less than 0.01 and an absolute normalized enrichment score (NES) of 1.5 or higher are shown, while for L p-value less than 0.05 and NES of 0.5 or higher were used. **(M-N-O)** Scatter plots representing the leading-edge genes that contribute to the upregulation of specific hallmark pathways in a given cluster relative to the remaining macrophages. **(M)** Scatter plots show the leading edge of the hallmark IFN-α response (top) and IFN-γ response (bottom) where red dots are genes exclusive to #3 Nos2+ MCT-12h, pink dots are genes exclusive to #1 Cxcl10+ TAMono, and grey dots are genes present in both clusters. **(N)** Scatter plots show the leading edge of the hallmark IFN-α response (top) and IFN-γ response (bottom) where red dots are genes exclusive to #3 Nos2+ MCT-12h, yellow-orange dots are genes exclusive to #6 S100a9/8+ TAM, and grey dots are genes present in both clusters. **(O)** Scatter plots show the leading edge of the hallmark inflammatory response (top) and TNF-α signaling via NF-κB (bottom) where red dots are genes exclusive to #3 Nos2+ MCT-12h, yellow-orange dots are genes exclusive to #6 S100a9/8+ TAM, and grey dots are genes present in both clusters.

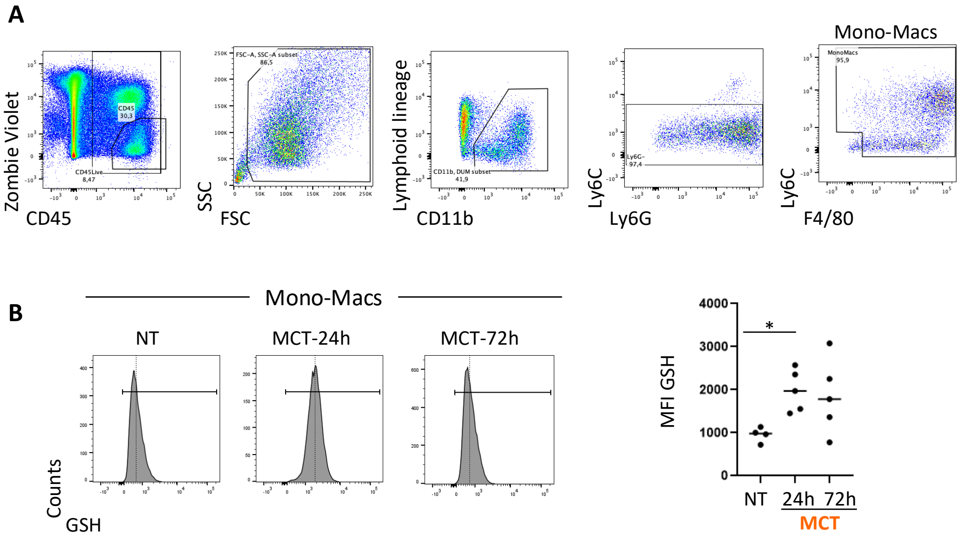

Supplementary Figure 7: Validation of cell defence against oxidative stress in *in vivo* MCT-activated macrophages.

Supplementary Figure 7 – Validation of cell defence against oxidative stress in *in vivo* MCT-activated macrophages.

Wild type mice were injected with tumor cells and treated with MCT when tumors reached 50–100 mm². **(A)** Representative flow cytometry gating strategy to identify (lymphoid Lineage- CD11b+ Ly6G- Ly6C+/- F4/80+/-) mono-macrophage subsets. This example is derived from a one day post-MCT (MCT-24h). **(B)** Representative flow cytometry histograms showing GSH level (thiol-tracker violet intensity) in NT (not-treated), one day post-MCT (MCT-24h) and three days post-MCT (MCT-72h). The dot plot on the right shows cumulative data with 4 to 5 animals per groups.

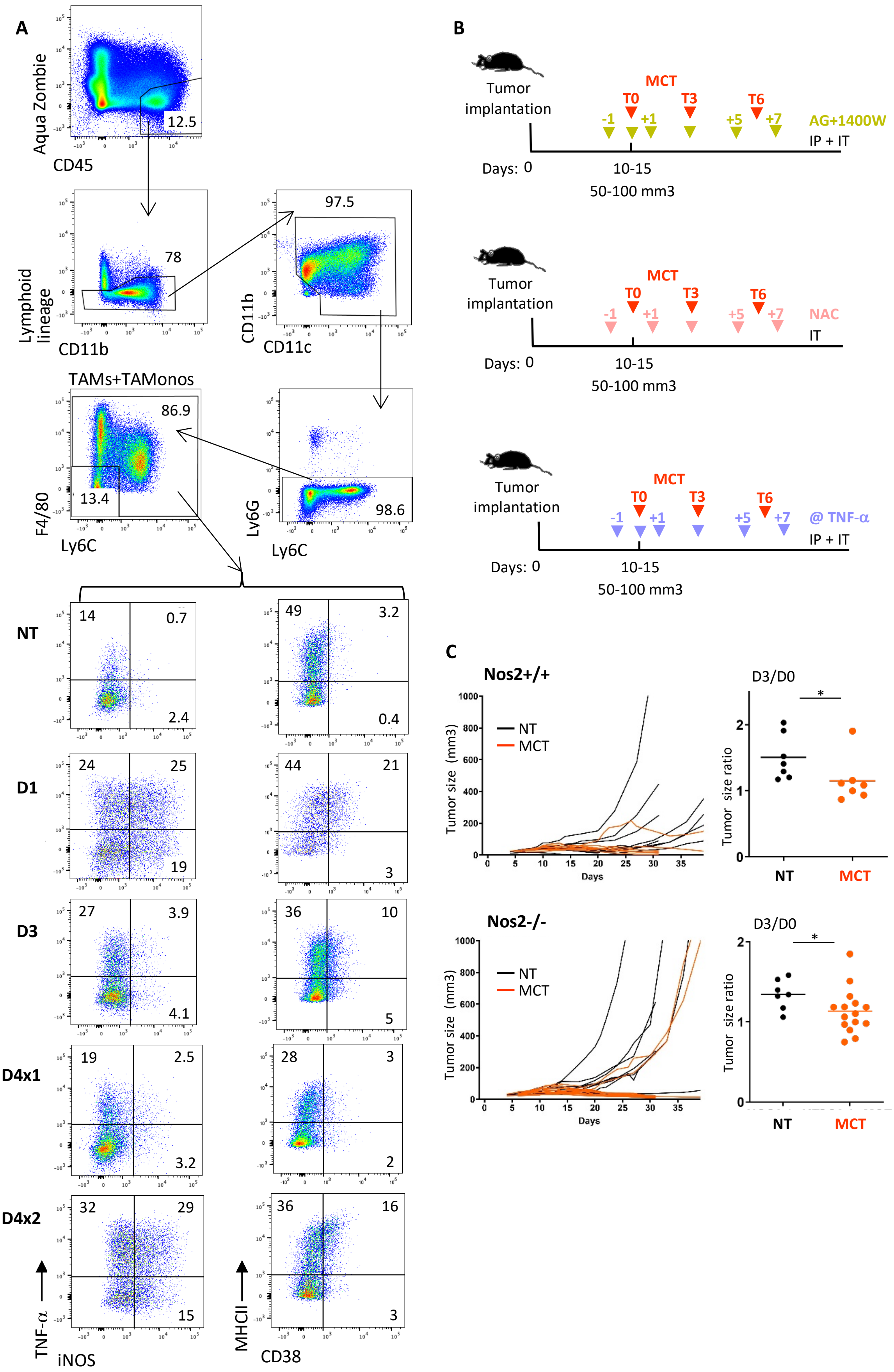

Supplementary Figure 8: FACS gating strategy of myeloid population responding to MCT and functional analysis.

Supplementary Fig. 8. Flow cytometry gating strategy of myeloid population responding to MCT and functional analysis.

(A) Representative flow cytometry plot and gating strategy to study tumor-infiltrated macrophages and monocytes. We collectively gated on myeloid cells identified as CD3e-CD19-NK1.1- cells, successively excluding CD11c-CD11b-double-negative cells, then Ly6G+ cells, and finally Ly6C-F4/80-double-negative cells (TAMs + TAMonos). To detect intracellular TNF-α production, tumor cell suspensions were restimulated with LPS+IFN-γ in vitro for 4 hours. Cell surface expression of MHC-II and CD38 was assessed on non-restimulated cells. Note that similar iNOS expression was obtained from cells whether they were restimulated or not. TAMs + TAMonos cells were isolated from NT, D1, D3, D4 x1, and D4 x2 animals. Flow cytometry plots are representative of TNF-α/iNOS and MHC-II/CD38 co-expressions. **(B)** Scheme of *in vivo* experiment setup for iNOS inhibition with 1400W and Aminoguanidine Hydrochloride, N-acetyl cysteine (NAC), and anti-mouse TNF-α blocking antibody. **(C)** Mice were injected with tumor cells and treated with MCT when tumors reached 50–100 mm². Individual tumor growth curves with or without MCT are shown for *Nos2* +/+ mice (top) and *Nos2* -/- mice (bottom). The graphs on the right side represent the ratio of tumor size at the time of treatment (T0) and three days later (T3/T0) for each individual mouse.

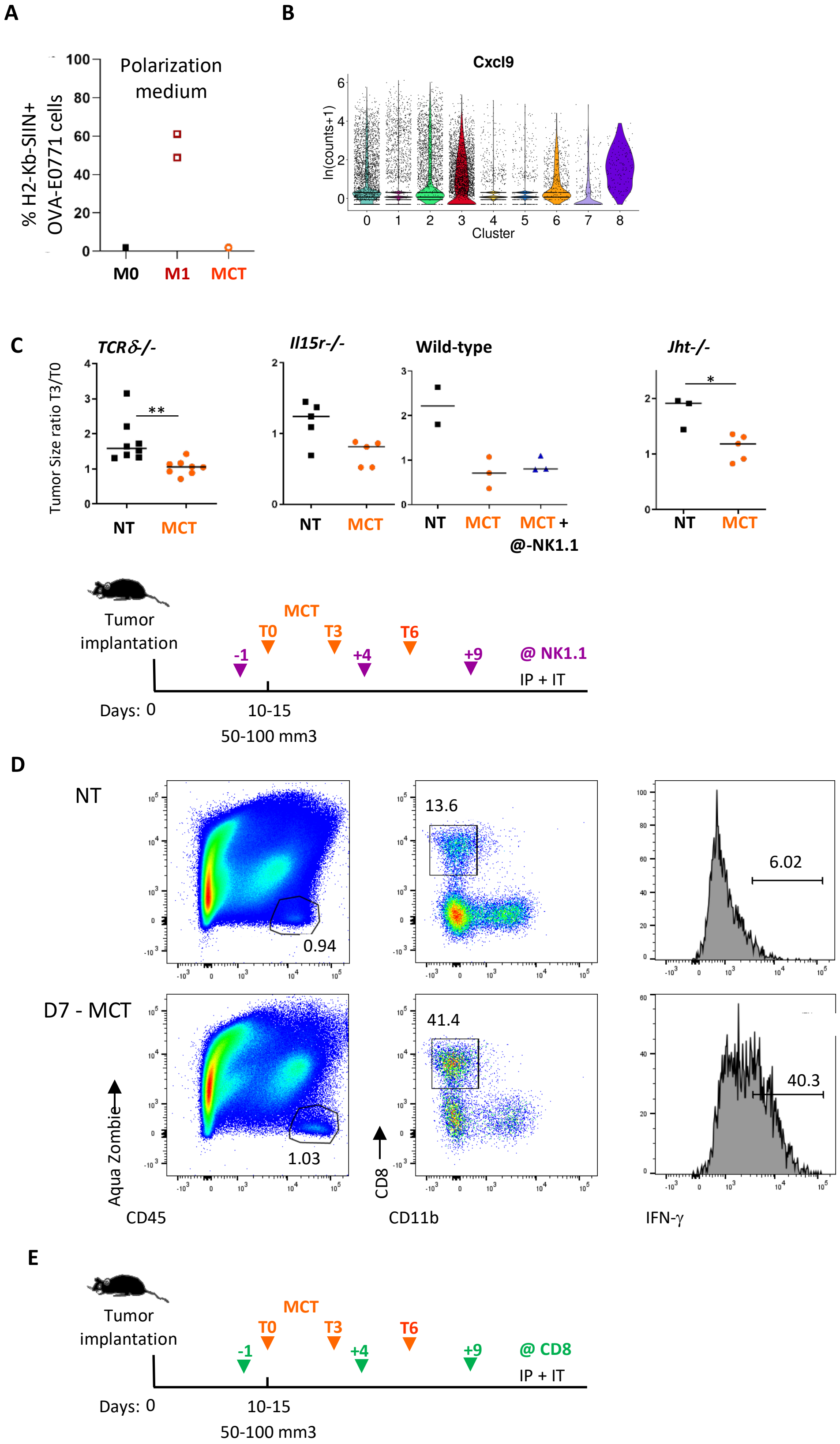

Supplementary Figure 9: Self-antigen presentation tumor cells and T cell activation *in vivo*.

Supplementary Fig. 9. Self-antigen presentation by tumor cells and T cell activation *in vivo*.

(A) Expression of H-2Kb-SIINFEKL complexes in OVA-E0771 cells incubated overnight with the polarizing medium M0, or M1 (LPS + IFN-γ), or MCT (TLR3 ligand Poly I:C + anti-CD40 antibody). **(B)** Violin plot showing normalized and log-transformed expression of *Cxcl9* for the nine tumor-infiltrating macrophage and monocyte clusters. **(C)** Ratio of tumor size three days post-MCT (T3/T0) in mice lacking γδ T cells (TCRδ KO mice), or lacking or depleted in NK cells (*Il15r* KO or wild-type mice receiving depleting anti-mouse NK1.1 antibody), or lacking B cells (*Jht* KO mice). Note that the scheme represents the *in vivo* experiment setup for NK cell depletion using depleting anti-mouse NK1.1 antibody. **(D)** Representative flow cytometry plots of tumors harvested from animals left untreated or that received MCT 7 days previously. CD8 T cells were gated as CD45+ CD8+ CD11b- cells, out of which the proportion of IFN-γ-producing cells was assessed. To detect intracellular IFN-γ production, tumor cell suspensions were restimulated with PMA + Ionomycin *in vitro* for 4 hours. **(E)** Scheme of *in vivo* experiment setup for CD8 T cell depletion using depleting anti-mouse CD8 antibody.